Inorganic Chemistry

Article

pubs.acs.org/IC

Structural, Magnetic, and Redox Diversity of First-Row Transition Metal Complexes of a Pyridine-Based Macrocycle: Well-Marked Trends Supported by Theoretical DFT Calculations

Bohuslav Drahoš, Radovan Herchel, and Zdeněk Trávníček*

Department of Inorganic Chemistry, Regional Centre of Advanced Technologies and Materials, Faculty of Science, Palacký University, 17. listopadu 12, CZ-771 46 Olomouc, Czech Republic

Supporting Information

ABSTRACT: A series of first-row transition metal complexes with 15-membered pyridine-based macrocycle (3,12,18-triaza-6,9-dioxabicyclo[12.3.1]octadeca-1(18),14,16-triene = **L**) was prepared ($[M^{II}(L)Cl_2]$, where M = Mn, Co, Ni, Zn (**1**, **3**, **4**, **6**); $[Fe^{III}(L)Cl_2]Cl$ (**2**), $[Cu^{II}(L)Cl]Cl$ (**5**)) and thoroughly characterized. Depending on the complexated metal atom, the coordination number varies from 7 (Mn, Fe, Co), through 5 + 2 for Ni and 4 + 1 for Cu, to 5 for Zn accompanied by changes in the coordination geometry from the pentagonal bipyramid (**1**−**4**) to the square pyramid (**5** and **6**). Along the series, the metal−oxygen distances were prolonged in such manner that their bonding character was investigated, apart from X-ray structural analysis, also by ab initio calculations (Mayer's bond order, electron localization function), which confirmed that, in **4** and **5**, two and one oxygen donor atoms are semicoordinated, respectively, and one and two oxygen atoms are uncoordinated in **5**, and **6**, respectively. On the basis of the temperature variable magnetic susceptibility measurements, **1** and **2** behave as expected for $3d^5$ high-spin configuration with negligible zero-field splitting (ZFS). On the other hand, a large axial ZFS (D(Co) ≈ 40 cm^{-1}, D(Ni) ≈ −6.0 cm^{-1}) was found for **3** and **4**, and rhombic ZFS (E/D ≈ 0.15) for **4**. Antiferromagnetic exchange coupling was observed for **4** and **5** (J(Ni) = −0.48 cm^{-1}, and J(Cu) = −2.43 cm^{-1}, respectively). The obtained results correlate well with ab initio calculations of ZFS parameters as well as J-values, which indicate that the antiferromagnetic exchange is mediated by hydrogen bonds. The complexes were also investigated by cyclic voltammetry in water or acetonitrile. A quasi-reversible couple Mn(II)/Mn(III) at 1.13/0.97 V, an almost reversible couple Fe(II)/Fe(III) at 0.51/0.25 V, and a one-step/multistep reduction/oxidation of Cu(II) complex **5** at −0.33 V/0.06−0.61 V were detected.

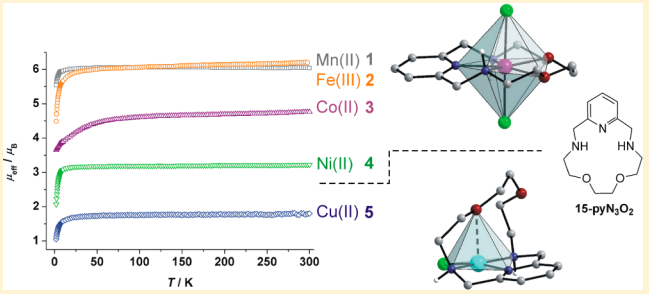

INTRODUCTION

Pyridine-containing macrocycles, in which the pyridine unit represents a part of the macrocyclic scaffold, are widely studied compounds due to their specific coordination abilities. Among such a large number of macrocycles with a different size of the macrocyclic cavity, that is, varying from 12 to 20 ring members and variable donor atoms, our attention has been devoted mainly to the derivatives of 15-membered macrocyclic ligands containing three nitrogen and two oxygen donor atoms in the ligand scaffold. The most common representatives of these ligands are in complexes whose X-ray crystal structures are the most abundant in the Cambridge Structural Database (CSD);[1] they are shown in Figure 1. According to the decreasing number of references regarding each of the compounds, including the metal complexes, they can be ordered as follows: 15-pydienN_3O_2,[2−18] 3,12,18-triaza-6,9-dioxabicyclo[12.3.1]-octadeca-1(18),14,16-triene (15-pyN_3O_2, **L**),[19−22] 15-pydion-N_3O_2,[23−26] Me_2-15pyN_3O_2,[27,28] (15-pydienN_3O_2)$_2$,[29] **L1**, and **L2**.[30] The above-mentioned ligands were used to complex different d-block transition metals as well as f-block lanthanides, and usually crystal structures and magnetic properties in the solid state were investigated, but also some experiments in solution regarding their redox properties,[2] their thermodynamic/kinetic stabilities,[28] or their efficiency as magnetic resonance imaging (MRI) contrast agents were performed.[22]

The most variable group of compounds is that of the metal complexes of 15-pydienN_3O_2. The mononuclear complexes with Mg(II), Fe(II), Mn(II), and Co(II), as well as with Y(III)[6] or few lanthanides,[7] were prepared. Usually the coordination number (CN) of 7 was found in the complexes, and the two axial positions of the pentagonal bipyramidal coordination sphere were occupied by different small monovalent ligands, for example, Cl^-, H_2O, SCN^-, or CN^- (Figure 2). Concerning the mononuclear complexes, the main attention was devoted to [Fe(15-pydienN_3O_2)$(CN)_2$]·H_2O, which shows spin crossover with the spin transition temperature of 159 K[4,8] and light-induced electron spin state trapping effect (LIESST) at $T_{(LIESST)}$ = 135 K related to one reversible iron−oxygen bond break.[13] The most recent research has been focused on

Received: December 22, 2014
Published: March 11, 2015

DOI: 10.1021/ic503054m
Inorg. Chem. 2015, 54, 3352−3369

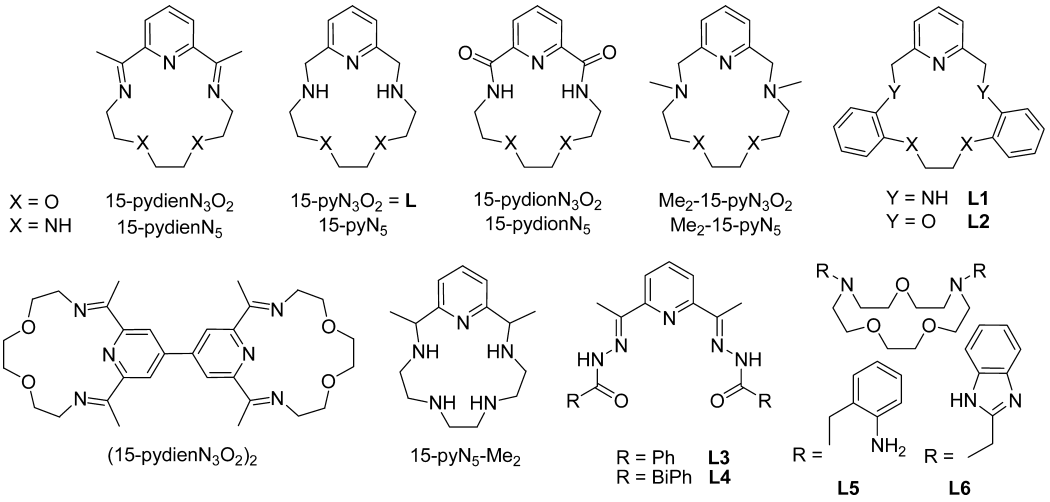

Figure 1. Structural formulas of the most common and discussed 15-membered pyridine-containing ligands with five donor atoms in the ligand scaffold and other selected ligands providing heptacoordination in their metal complexes.

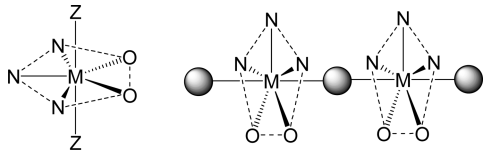

Figure 2. Schematic illustration of coordination modes of discussed ligands previously observed in mononuclear (left) and polynuclear (right) complexes. The dashed lines connecting the donor atoms represent the ligand scaffold. Z = a small monodentate ligand, M = variable metal atom, spheres represent different types of cyanidometallates: $[M^{I}(CN)_2]$, $[M^{II}(CN)_4]^{2-}$, $[M^{III}(CN)_6]^{3-}$ (M^{I} = Ag, Au; M^{II} = Ni, Pd, Pt; M^{III} = Fe, Cr, Co).

polynuclear heterometallic one-dimensional (1D) chains or two-dimensional (2D) layers formed upon axial coordination of bidentate bridging units particularly based on cyanidometallates (Figure 2). The cyanido-bridged $[Mn^{II}-M^{II/III}-Mn^{II}]$ heterotrinuclear complexes were prepared by bridging the [Mn(15-pydienN$_3$O$_2$)] building block by $[M(CN)_6]^{4-/3-}$ where M = Fe(II),[9] Fe(III), Cr(III), Co(III).[12] An antiferromagnetic exchange interaction was found between Mn(II) and Cr(III), and a ferromagnetic one was found between Mn(II) and Fe(III). When the same [Mn(15-pydienN$_3$O$_2$)] building block was bridged by $[M(CN)_2]^-$, where M = Au(I) or Ag(I),[16] heterometallic 1D chains were formed, and a very weak antiferromagnetic interaction between neighboring Mn(II) atoms bridged by the diamagnetic NC−M−CN unit was observed. Using $[M(CN)_4]^{2-}$, where M = Ni(II), Pd(II), Pt(II) as a bridging unit, gave rise to a 1D chain without any significant magnetic interaction between Mn(II) atoms.[9]

Besides Mn(II), other metal ions were also complexated by 15-pydienN$_3$O$_2$; for example, Fe(II) in a cyanido-bridged $Fe^{II}-Mn^{II}$ 1D chain exhibited spin crossover as well as LIESST effect,[10] and Co(II) in $[Co^{II}$(15-pydienN$_3$O$_2$)$]_2[Cr^{III}(CN)_6]$ trinuclear complex, which self-assembled into chiral nanotubular structure, which consists of interlocked single and double helices, exhibited ferromagnetic coupling between Co(II) and Cr(III) (J = 1.2 cm^{-1}) and ferromagnetic ordering below 12 K.[17] The trinuclear complex based on two $[Fe^{II}$(15-pydienN$_3$O$_2$)(H$_2$O)] units bridged by $[Cr(CN)_6]^{3-}$ was found to be the first Fe(II) cyanido-bridged single-molecule magnet (SMM) with a large anisotropy barrier (U_{eff} = 44.3 K).[18] Except for cyanidometallates, other bridging units were used to connect the pentagonal [M(15-pydienN$_3$O$_2$)] planes (derivatives of 1,2-bis(pyridine-2-carboxamido)benzenate[14] or $[Fe(salen)(CN)_2]^-$, where H$_2$salen = *N*,*N*′-bis(salicyl)-ethylenediamine).[15]

To the best of our knowledge, there exist only two Mn(II) complexes of **L**.[22] Their structures are similar to those with 15-pydienN$_3$O$_2$ with the coordination number of 7 for Mn(II) and two chlorides or one chloride and one water molecule coordinated in the axial positions of the pentagonal bipyramid. Additional characterization of the complexes was performed only in solution (characterization of potential MRI contrast agents), magnetic properties were described by NMR measurements, and quasi-reversible oxidation at high potential 1.2 V (vs standard hydrogen electrode (SHE)) in aqueous solution was found.[22] Only one complex of a bimacrocyclic ligand (15-pydienN$_3$O$_2$)$_2$ with Mn(II) was previously described,[29] with CN of 7 for Mn(II) and one water molecule and one chlorido ligand in axial positions. The investigation of magnetic properties revealed a weak intramolecular antiferromagnetic exchange between the two Mn(II) atoms. In the case of more rigid ligands **L1** and **L2**, their Cu(II), Co(II), and Ni(II) complexes were studied; mainly, the influence of the arrangement of the donor atoms in the ligand on the thermodynamic stability of Cu(II) complexes (complex with **L1** was more stable than that with **L2**) and crystal structures of Cu(II) and Ni(II) complexes of **L2** with CN of 6 for both metals was described.[30]

The 15-pydionN$_3$O$_2$ ligand was studied previously only in the case of a Ca(II) complex, in which Ca(II) is situated outside the macrocyclic cavity and coordinated by four amide-oxygen atoms coming from four ligands.[24] Next work was done on structurally similar ligand 15-pydionN$_5$ having five nitrogen donor atoms in the ligand scaffold whose Fe(II) and Fe(III) complexes with pentagonal bipyramidal geometry were prepared.[31,32] In the Fe(III) complex, a high-spin (HS) state and spin crossover to a long-range antiferromagnetic order at T < 3.2 K occurred. The negatively charged deprotonated amide groups stabilized the oxidation state +III of iron ($E(Fe^{III}\mathbf{L}/Fe^{II}\mathbf{L})$ = −0.57 V vs standard calomel electrode (SCE)).[31] Similarly in the Fe(II) complex, Fe(II) was found in HS state all over the temperature range without any long-range magnetic

DOI: 10.1021/ic503054m
Inorg. Chem. 2015, 54, 3352−3369

ordering at low temperature, and the measured redox potential was identical to that for Fe(III) complex.[32]

Besides the 15-membered pyridine-based macrocycles discussed above, other ligands (Figure 1, **L3**−**L6**), whose complexes have a rather unusual heptacoordinated central transition metal atom, were described previously. It has been found that mononuclear Co(II) and Ni(II) complexes of the pyridine-based Schiff bases **L3** and **L4**[33,34]or derivatives of 1,10-diaza-15-crown-5 **L5** and **L6**[35] show large magnetic anisotropy demonstrated by a large positive and negative value of axial zero-field splitting (ZFS) parameter for Co(II), and Ni(II), respectively.[33,35] On the basis of the negative *D*-value for Ni(II) complexes of **L3** and **L4**, the building unit $[Ni(\mathbf{L3})]^{2+}$/$[Ni(\mathbf{L4})]^{2+}$ was combined with $[W(CN)_8]^{3-}$ forming a pentanuclear $\{Ni_3W_2\}$ complex that behaved as a single-chain-magnets (SCM).[36]

In this paper, the coordination ability of a rarely utilized 15-membered pyridine-based macrocyclic ligand **L** is investigated on a new series of complexes of selected first-row transition metals (Mn(II), Fe(III), Co(II), Ni(II), Cu(II), and Zn(II)), because no complexes of this ligand, except for two complexes with Mn(II),[22] were described previously. The determined molecular and crystal structures of all the complexes are discussed in detail and correlated with their magnetic properties in the solid state. The experimentally obtained findings are compared with results of ab initio calculations regarding the chemical bonding between metal atoms and the ligands donor atoms, the ZFS tensor parameters, and the intermolecular magnetic interactions. The magnetic data in solid state are compared with those in solution, and the redox behavior of the studied complexes is investigated by cyclic voltammetry. Thorough characterization of this series possesses an observation of several well-marked trends and correlations, which could give better insight into the coordination chemistry and magnetochemistry of complexes with pyridine-based macrocyclic ligands and which would help in the seeking of compounds with desirable magnetic properties and application potential.

EXPERIMENTAL SECTION

Materials and Syntheses. The ligand **L** was synthesized according to the literature procedure described elsewhere.[22] All the solvents (Penta, Prague, Czech Republic) and other chemicals were purchased from commercial sources (Across Organics, Geel, Belgium and Sigma Aldrich, St. Louis, MO, USA) and used as received.

*[Mn(L)Cl$_2$] (**1**).* **L** (0.250 g, 1.00 mmol) was dissolved in 25 mL round-bottom flask in 2.5 mL of methanol (MeOH). The solution of $MnCl_2{\cdot}4H_2O$ (0.195 g, 1.00 mmol) in 2.5 mL of MeOH was added, and the mixture was heated under reflux for 5 min. If any precipitate formed, it was filtered through Millipore syringe filter (0.45 μm). Diethylether (Et_2O) was slowly added dropwise to a stirred solution of the complex until precipitate formed and the color of the solution faded. The precipitate was removed by filtration on a glass frit, washed twice with 10 mL of Et_2O, and stored in vacuum desiccator over KOH for 2 d. The complex was obtained as pale brown powder (0.22 g, yield 55.7%). Mass spectrometry (MS) *m*/*z* (+): 341.08 $[Mn(\mathbf{L})Cl]^+$. Anal. Calcd (%) for $C_{13}H_{21}Cl_2N_3O_2Mn{\cdot}H_2O$ (**1**·H_2O): C, 39.51; H, 5.87; N, 10.63. Found C, 39.65; H, 5.48; N, 10.19.

*[Fe(L)Cl$_2$]Cl (**2**).* All the complexes were prepared similar to the procedure described above for the Mn(II) complex (**1**). The product was obtained as a dark yellow crystalline solid (0.26 g, yield 55.6%). MS *m*/*z* (+): 305.02 $[Fe(\mathbf{L}-2H)]^+$, 340.98 $[Fe(\mathbf{L}-H)Cl]^+$, 376.94 $[Fe(\mathbf{L})Cl_2]^+$. Anal. Calcd (%) for $C_{13}H_{21}Cl_3N_3O_2Fe{\cdot}3H_2O{\cdot}CH_3OH$ (**2**·$3H_2O{\cdot}CH_3OH$): C, 33.66; H, 6.25; N, 8.41. Found: C, 33.40; H, 6.12; N, 8.53.

*[Co(L)Cl$_2$] (**3**).* The product was obtained as a violet powder (0.24 g, 60.1%). MS *m*/*z* (+): 345.05 $[Co(\mathbf{L})Cl]^+$. Anal. Calcd (%) for $C_{13}H_{21}Cl_2N_3O_2Co{\cdot}H_2O$ (**3**·H_2O): C, 39.12; H, 5.81; N, 10.53. Found: C, 39.14; H, 5.46; N, 10.13.

*[Ni(L)Cl$_2$] (**4**).* The product was obtained as a green powder (0.20 g, yield 52.5%). MS *m*/*z* (+): 344.02 $[Ni(\mathbf{L})Cl]^+$. Anal. Calcd (%) for $C_{13}H_{21}Cl_2N_3O_2Ni$ (**4**): C, 40.99; H, 5.56; N, 11.03. Found: C, 40.72; H, 5.66; N, 10.62.

*[Cu(L)Cl]Cl (**5**).* The product was obtained as a dark blue crystalline solid (0.20 g, yield 51.8%). MS *m*/*z* (+): 349.00 $[Cu(\mathbf{L})Cl]^+$, 734.89 $[Cu_2(\mathbf{L})_2Cl_3]^+$. Anal. Calcd (%) for $C_{13}H_{21}Cl_2N_3O_2Cu$ (**5**): C, 40.47; H, 5.49; N, 10.89. Found: C, 40.11; H, 5.80; N, 10.66.

*[Zn(L)Cl$_2$] (**6**).* The product was obtained as a white microcrystalline solid (0.21 g, yield 68.2%). MS *m*/*z* (+): 314.24 $[Zn(\mathbf{L}-H)]^+$, 350.27 $[Zn(\mathbf{L})Cl]^+$. Anal. Calcd (%) for $C_{13}H_{21}Cl_2N_3O_2Zn$ (**6**): C, 40.28; H, 5.46; N, 10.84. Found: C, 40.26; H, 5.55; N, 10.27.

Physical Methods. Elemental analysis (C, H, N) was performed on a Flash 2000 CHNO-S Analyzer (Thermo Scientific, Waltham, MA, USA). Infrared (IR) spectra of the complexes were recorded on a Thermo Nicolet NEXUS 670 FT-IR spectrometer (Thermo Nicolet, Waltham, MA, USA) employing the ATR technique on a diamond plate in the range of 400−4000 cm^{-1}. The mass spectra were collected on an LCQ Fleet Ion Mass Trap mass spectrometer (Thermo Scientific, Waltham, MA, USA) equipped with an electrospray ion source and three-dimensional (3D) ion-trap detector in the positive mode. Simultaneous thermogravimetry (TG) and differential thermal analysis (DTA) were carried out using an Exstar TG/DTA 6200 thermal analyzer (Seiko Instruments Inc., Torrance, CA, USA) with a dynamic air atmosphere (100 mL min^{-1}) in the temperature interval of 25−900 °C with the heating rate 5.0 °C min^{-1}. Temperature dependence of the magnetization at B = 0.1 or 1.0 T from 1.9 to 300 K and the isothermal magnetizations at T = 2.0 and 5.0 K up to B = 5 T were measured using MPMS XL-7 SQUID magnetometer (Quantum Design Inc., San Diego, CA, USA). The experimental data were corrected for diamagnetism.[37]

X-ray Diffraction Analysis. Single crystals of complexes **1**·$2CH_3OH$, **2**·$2H_2O$, **3**·$2CH_3OH$, **4**, **5**, and **6** suitable for X-ray analysis were prepared by a vapor diffusion of Et_2O into the MeOH solution of the appropriate complex at 5 °C, except for the complex **6**, which crystallized when its hot aqueous solution cooled to room temperature. X-ray single-crystal diffraction experiments for all the complexes were performed on an Oxford Diffraction Xcalibur2 diffractometer equipped with a Sapphire2 CCD detector using Mo Kα radiation. The CrysAlis software package (Version 1.171.33.52, Oxford Diffraction Ltd.)[38] was used for data collection and reduction. The molecular structures were solved by direct methods and refined by full-matrix least-squares techniques using SHELX97.[39] All non-hydrogen atoms of all the complexes were refined anisotropically. Hydrogen atoms of all the compounds were found in the difference Fourier maps and refined using a riding model, with C−H = 0.95 $(CH)_{ar}$, C−H = 0.99 (CH_2), and C−H = 0.98 (CH_3) Å and with $U_{iso}(H) = 1.2U_{eq}(CH, CH_2)$ and $1.5U_{eq}(CH_3)$, except for those belonging to N−H groups, which were refined freely in most cases. The Ni, Cl1, and Cl2 atoms in **4** are disordered over two positions with the occupancy factors of 0.876(7) and 0.124(7). The structures of all the studied complexes, depicted in Figures 3, 4, 5, 6 and Supporting Information, Figure S3, were drawn using the Mercury and Diamond software.[40]

Theoretical Methods. The ab initio theoretical calculations were performed using the ORCA 3.0.1 computational package.[41] The relativistic effects were included in all the calculations using the scalar relativistic contracted version of def2-TZVP(-f) basis functions[42] and with zero order regular approximation (ZORA).[43]

The single-point energy calculations based on X-ray geometries were done using the B3LYP functional.[44] The isotropic exchange constants J were calculated by comparing the energies of HS and broken-symmetry (BS) spin states utilizing both Ruiz's approach[45] and Yamaguchi's approach[46] by comparing the energies of HS and BS spin states. In all the cases the calculations were based on the experimental X-ray structures, but the hydrogen atom positions were optimized when these atoms were involved in a magnetic coupling path using the

DOI: 10.1021/ic503054m
Inorg. Chem. 2015, 54, 3352−3369

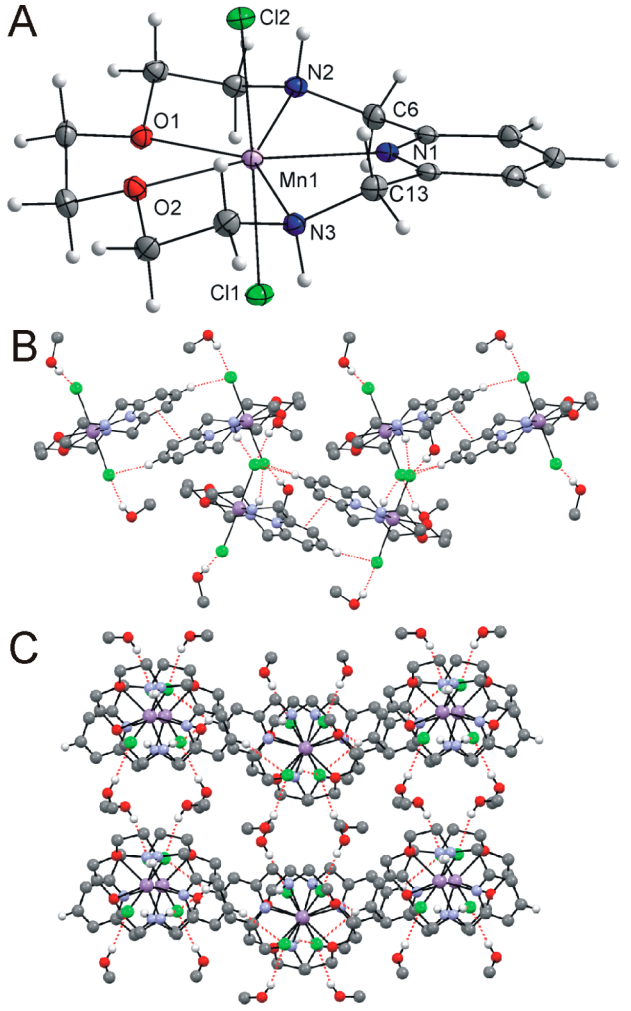

Figure 3. (A) Molecular structure of $[Mn(\mathbf{L})Cl_2]\cdot 2CH_3OH$ (**1**·$2CH_3OH$). The solvent molecules were omitted for clarity. Non-hydrogen atoms are drawn as thermal ellipsoids at the 50% probability level. (B) Part of the crystal structure of **1**·$2CH_3OH$ showing $\pi-\pi$ stacking and N−H···Cl, O−H···Cl, and C−H···Cl noncovalent contacts (red dashed lines, view along *c* axis). (C) View on the packing of the 2D-sheet structure in **1**·$2CH_3OH$ (red dashed lines represent the above-mentioned contacts). Hydrogen atoms not involved in these contacts were omitted for clarity.

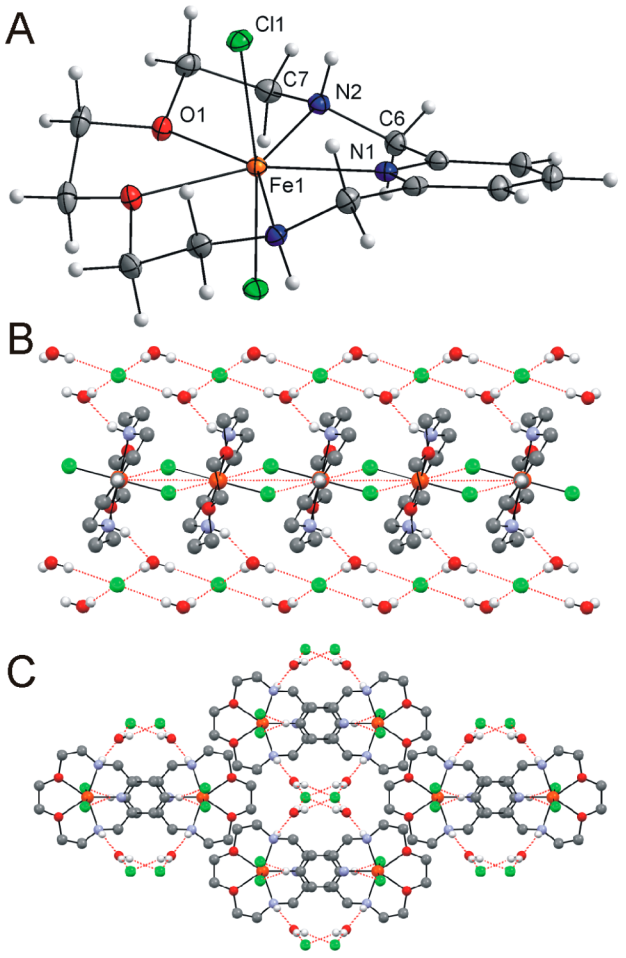

Figure 4. (A) Molecular structure of the $[Fe(\mathbf{L})Cl_2]^+$ complex cation in $[Fe(\mathbf{L})Cl_2]Cl\cdot 2H_2O$ (**2**·$2H_2O$). The crystal water molecules and chloride counterion were omitted for clarity. Non-hydrogen atoms are drawn as thermal ellipsoids at the 50% probability level. (B) Part of the crystal structure of **2**·$2H_2O$ showing $\pi-\pi$ stacking and N−H···O, O−H···Cl, and C−H···Cl noncovalent contacts (red dashed lines, view along *b* axis). (C) View on the packing of **2**·$2H_2O$ down the *c* axis (red dashed lines represent the above-mentioned contacts). Hydrogen atoms not involved in these contacts were omitted for clarity.

B3LYP functional and atom-pairwise dispersion correction to the density functional theory (DFT) energy with the Becke−Johnson damping (D3BJ).[47]

The calculations of ZFS parameters were performed using state average complete active space self-consistent field (SA-CASSCF)[48] wave functions complemented by N-electron valence second order perturbation theory (NEVPT2).[49] The active spaces of the CASSCF calculations on metal-based d-orbitals were defined as follows: CAS(5,5) for Mn(II) and Fe(III), CAS(7,5) for Co(II), CAS(8,5) for Ni(II), and CAS(9,5) for Cu(II). In the state-averaged approach all multiplets for given electron configuration were equally weighted. The ZFS parameters, based on dominant spin−orbit coupling contributions from excited states, were calculated through quasi-degenerate perturbation theory (QDPT),[50] in which an approximation to the Breit−Pauli form of the spin−orbit coupling operator (SOMF approximation)[51] and the effective Hamiltonian theory[52] were utilized.

All the above-mentioned calculations utilized the resolution of identity (RI) approximation with the decontracted auxiliary def2-TZV/J or def2-TZV/C Coulomb fitting basis sets and the chain-of-spheres approximation to exact exchange.[53] Increased integration grids (Grid5 for DFT and Grid4 for CASSCF in ORCA convention) and tight SCF convergence criteria were used in all calculations.

The Multiwfn 3.3.5 (A Multifunctional Wavefunction Analyzer)[54] was used to analyze the results from single-point energy calculations (B3LYP+ZORA/def2-TZVP(-f)) to quantify bond order using Mayer's bond analysis[55] and also by electron localization function (ELF)[56] based on topology analysis technique proposed by Bader.[57]

The spin densities were visualized with the help of program GABEDIT[58] and POV-Ray.[59]

Solution Studies. The bulk magnetic susceptibility (BMS) measurements were performed on a 400 MHz Varian spectrometer at 298 K. Samples in 5 mm NMR tubes contained 5 mM complex and 5% *t*-butanol by volume in D_2O (or CD_3OD) and an insert NMR tube containing 5% *t*-butanol by volume in D_2O (or CD_3OD).

The cyclic voltammetry was performed on electrochemical analyzer CHI600C (CH Instrument Inc., Austin, TX, USA). A conventional electrochemical three-electrode-type cell was used with a Ag/AgCl or Ag/Ag^+ reference electrode, a platinum wire auxiliary electrode, and a glassy carbon working electrode. The final potential values referred to SHE were obtained using the relation between the two reference electrodes: Ag/AgCl electrode (saturated KCl) versus SHE = +198 mV or using internal ferrocene/ferrocenium standard ($E_{1/2}$ = 0.665 V). The measurements were performed in aqueous solutions in the

DOI: 10.1021/ic503054m
Inorg. Chem. 2015, 54, 3352−3369

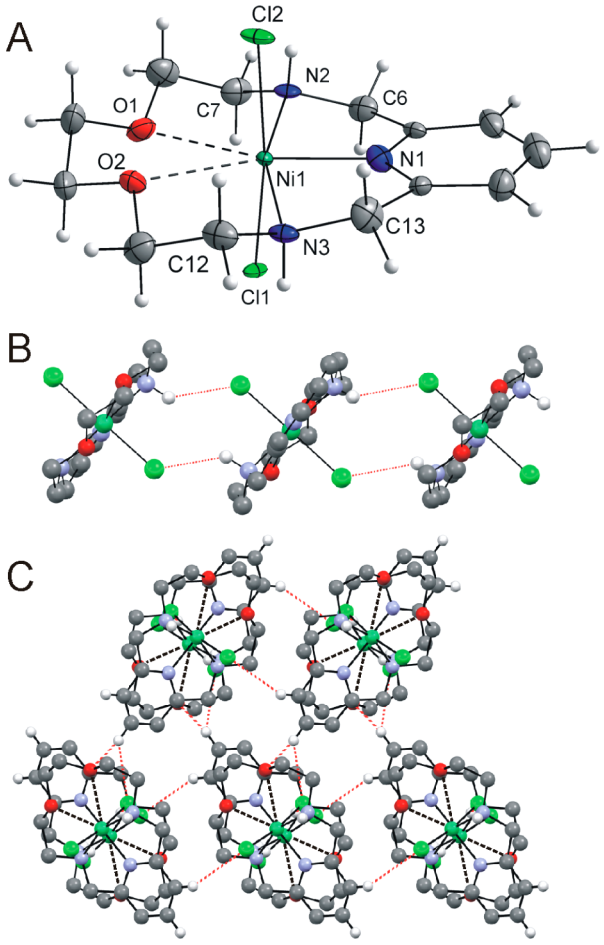

Figure 5. (A) Molecular structure of $[Ni(\mathbf{L})Cl_2]$ (**4**), the second parts of the disordered Ni and Cl atoms are omitted for clarity. The dashed lines between Ni and O atoms represent semicoordination. Non-hydrogen atoms are drawn as thermal ellipsoids at the 50% probability level. (B) Part of the crystal structure of **4** showing N−H···Cl hydrogen bonds (red dashed lines). (C) View on the packing of **4** (red dashed lines represent N−H···Cl and C−H···Cl noncovalent contacts). Hydrogen atoms not involved in these contacts were omitted for clarity.

presence of 0.1 M KCl or in acetonitrile (MeCN) solution in the presence of 0.1 M tetrabutylammonium perchlorate (TBAP) as a supporting electrolyte with scan rate of 100 mV s^{-1} for 5×10^{-3} M concentration of the complexes.

RESULTS AND DISCUSSION

Syntheses and General Characterization. The ligand **L** was synthesized according to the previously described literature procedure.[22] All the complexes were prepared by the same procedure based on mixing free **L** and the appropriate metal halide in MeOH in an equimolar ratio and heating to reflux. Solid complexes precipitated from the solution upon addition of excess of Et_2O. The solubility of Mn(II), Co(II), Ni(II), and Zn(II) complexes (**1**, **3**, **4**, and **6**) in MeOH was higher than that of Fe(III) and Cu(II) complexes (**2** and **5**), which partially crystallized from MeOH after the solutions cooled to room temperature. Measured IR spectra of the ligand **L** and all the complexes revealed a similar pattern, as it is shown in Supporting Information, Figure S1 (a complete list of peaks for each complex can be found in Supporting Information), showing the presence of **L** within the complexes. They all contain two medium peaks at ∼1440 and ∼1470 cm^{-1} and a sharp doublet at 1600 and 1580 cm^{-1} corresponding to the wagging vibrations of the pyridine ring. Multiplets at ∼2900 cm^{-1} correspond to the CH_2 stretching vibrations, and the medium signal assigned to the stretching mode of the two NH groups is found at ∼3200 cm^{-1} (shifted by ∼100 cm^{-1} to lower wavenumbers upon coordination to the metal). Only in the spectrum of **2**, strong absorption bands between 3300 and 3500 cm^{-1} corresponding to the stretching vibrations of crystal water molecules and broad absorption band at 586 cm^{-1}, which could be assigned to the rocking vibration of water molecule connected to NH group via hydrogen bond,[4] have been observed. The results of simultaneous TG/DTA analyses in a dynamic air atmosphere are shown in Supporting Information, Figure S2 for two representative complexes **1** and **2**. In the temperature range of 25−170 °C, a weight loss corresponding to the elimination of half water molecule, one MeOH molecule, and half water solvate molecule(s) was observed for Mn(II) (**1**), Fe(III) (**2**), and Co(II) (**3**) complexes, respectively (endo effect in DTA curve at 120 °C was found only for **2**). Further thermal decomposition including loss of the rest of water solvate molecules proceeded in two/one step without formation of thermally stable intermediates but with several endo and exo effects. The decomposition was finished above 600 °C, and the final products were not studied in detail. The obtained results also indicated that the fast synthetic method (a precipitation by addition of Et_2O) gave complexes with different types and/or numbers of crystal solvent molecules, and thus this discrepancy can be seen looking to results of TG/DTA and X-ray structural data.

Description of Crystal Structures of 1−6. The molecular structures of all the complexes were determined using single-crystal X-ray diffraction analysis, and selected crystallographic data and structural refinement parameters are listed in Table 1.

Mn(II), Fe(III), and Co(II) Complexes (1, 2, and 3). Complexes **1**−**3** revealed similar molecular structures. The molecular structure of **1** is depicted in Figure 3a, while that of **2** is depicted in Figure 4a and that of **3** is in Supporting Information, Figure S3a. Selected structural parameters are listed in Table 2. In all three complexes, the central metal atom adopts pentagonal bipyramidal geometry with the N_3O_2 donor set forming a planar equatorial plane and two chlorido ligands coordinated in axial positions. The observed CN of 7 is typical for Mn(II) and Fe(III) complexes with the 15-membered pyridine-based macrocycles with five donor atoms (Figures 2, 3a, and 4a), while this CN is rather exceptional for Co(II) complexes. The M−N(pyridine) bond is the shortest from all coordination bonds in **1**−**3** (2.218(2), 2.155(2), and 2.136(2) Å for **1**, **2**, and **3**, respectively) which is a typical feature also for all other studied complexes **4**−**6**. In **1**, the M−N (aliphatic) and M−O bonds have very similar lengths (2.30−2.32 Å), while in **2** and **3** the M−N (aliphatic) distances are a bit shortened (∼0.05−0.1 Å) in comparison with the M−O distances. On the other hand, the pentagonal bipyramid is a little distorted in all the cases, because the axial M−Cl bonds are ∼0.1−0.2 Å longer than the other five coordination bonds to the central metal atom. Additionally, only Fe(III) complex unit has a real twofold rotation axis (C_2) lying on the Fe−N(pyridine) coordination bond.

The deformation of the pentagonal bipyramidal coordination environment around the central metal atom in the complex is usually described by the mean deviation value of all ligand donor atoms from the least-squares plane formed by central

DOI: 10.1021/ic503054m
Inorg. Chem. 2015, 54, 3352−3369

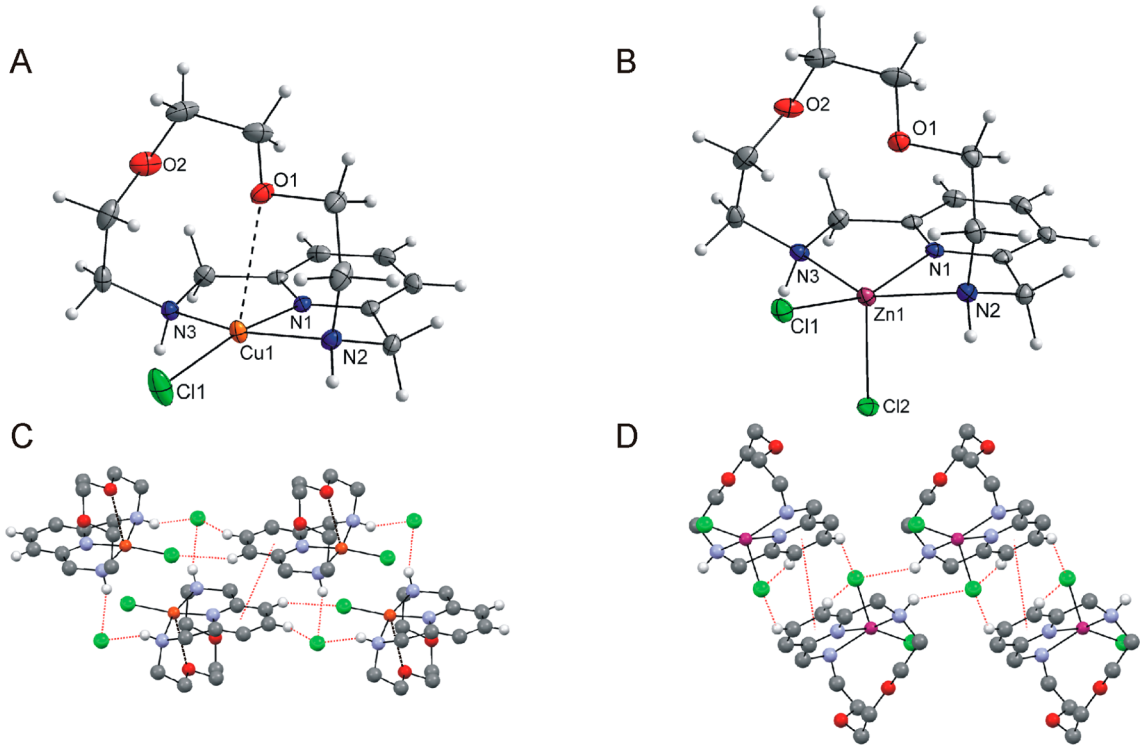

Figure 6. (A) Molecular structure of the $[Cu(L)Cl]^+$ complex cation in $[Cu(L)Cl]Cl$ (**5**). (B) Molecular structure of $[Zn(L)Cl_2]$ (**6**). Non-hydrogen atoms are drawn as thermal ellipsoids at the 50% probability level. (C, D) Part of the crystal structure of **5** or **6** showing $\pi-\pi$ stacking and N−H···Cl and C−H···Cl noncovalent contacts (red dashed lines). Hydrogen atoms not involved in these contacts were omitted for clarity.

Table 1. Crystallographic Parameters of the Studied Complexes

compound	**1**·2CH_3OH	**2**·2H_2O	**3**·2CH_3OH	**4**	**5**	**6**
formula	$C_{15}H_{29}Cl_2N_3O_4Mn$	$C_{13}H_{25}Cl_3N_3O_4Fe$	$C_{15}H_{29}Cl_2N_3O_4Co$	$C_{13}H_{21}Cl_2N_3O_2Ni$	$C_{13}H_{21}Cl_2N_3O_2Cu$	$C_{13}H_{21}Cl_2N_3O_2Zn$
M_r	441.25	449.56	445.24	380.94	385.77	387.60
color	colorless	yellow plate	violet	green	dark blue	colorless
crystal system	monoclinic	monoclinic	monoclinic	monoclinic	triclinic	triclinic
space group	$P2_1/n$	$C2/c$	$P2_1/n$	$P2_1/c$	$P\bar{1}$	$P\bar{1}$
a (Å)	10.1808(2)	9.2600(2)	10.0967(5)	13.0687(3)	9.3950(3)	7.6819(4)
b (Å)	16.0983(3)	22.2181(6)	16.0801(5)	7.63859(19)	9.6921(2)	9.1387(4)
c (Å)	12.7156(3)	9.0231(2)	12.6714(6)	16.8592(4)	9.8499(2)	11.5537(4)
α (deg)	90.00	90.00	90.00	90.00	82.7007(19)	91.215(3)
β (deg)	110.430(3)	90.231(2)	110.714(6)	101.070(3)	65.535(3)	92.602(3)
γ (deg)	90.00	90.00	90.00	90.00	77.518(2)	105.474(4)
U, Å^3	1952.92(8)	1856.40(8)	1924.30(14)	1651.69(7)	796.38(4)	780.42(6)
Z	4	4	4	4	2	2
D_{calc}, g cm^{-3}	1.501	1.609	1.537	1.532	1.609	1.649
μ, mm^{-1}	0.974	1.267	1.194	1.504	1.713	1.923
$F(000)$	924	932	932	792	398	400
reflections collected	18 083	8957	17 481	14 842	7573	7293
independent reflections	3435	1640	3378	2893	2805	2736
	[R(int) = 0.0243]	[R(int) = 0.0154]	[R(int) = 0.0206]	[R(int) = 0.0269]	[R(int) = 0.0182]	[R(int) = 0.0151]
data/restraints/ parameters	3435/0/228	1640/2/133	3378/0/238	2893/0/220	2805/0/198	2736/0/190
goodness-of-fit on F^2	1.064	1.091	1.060	1.116	1.048	1.083
R_1, wR_2 ($I > 2\sigma(I)$)[a]	0.0233/0.0633	0.0190/0.0524	0.0221/0.0584	0.0609/0.1689	0.0226 /0.0586	0.0197/0.0528
R_1, wR_2 (all data)[a]	0.0282/0.0646	0.0206/0.0531	0.0248/0.0593	0.0677/0.1729	0.0263/0.0594	0.0209/0.0531
largest diff. peak and hole, A^{-3}	0.318 and −0.276	0.298 and −0.168	0.332 and −0.232	2.320 and −0.441	0.337 and −0.212	0.309 and −0.252
CCDC number	1038350	1038349	1038347	1038351	1038348	1038352

[a] $R_1 = \sum(|F_o| - |F_c|)/\sum|F_c|$; $wR_2 = [\sum w(F_o^2 - F_c^2)^2/\Sigma w(F_o^2)^2]^{1/2}$.

metal and the donor atoms of the ligand. Its value for **1**, **2**, and **3** is 0.14, 0.05, and 0.13 Å, respectively, which documents that the best planar location of the plane-forming atoms is for **2** (Fe(III)), while in **1** and **3** (Mn(II) and Co(II)) it is ∼2.5

DOI: 10.1021/ic503054m
Inorg. Chem. 2015, 54, 3352−3369

Table 2. Selected Bond Lengths (Å) and Angles (deg) for All the Studied Complexes

distances	**1**·2CH_3OH	**2**·2H_2O	**3**·2CH_3OH	**4**	**5**	**6**
M−N1	2.2182(13)	2.1553(17)	2.1363(13)	1.987(4)	1.9250(15)	2.0855(13)
M−N2	2.3086(13)	2.2010(12)	2.2183(13)	2.132(3)	2.0258(15)	2.1858(13)
M−N3	2.3081(13)		2.2224(13)	2.118(3)	2.0305(15)	2.2363(13)
M−O1	2.3204(11)	2.2467(10)	2.3382(11)	2.663(3)	2.721(2)	3.113(1)
M−O2	2.2980(11)		2.3119(11)	2.506(3)	3.816(2)	4.030(1)
M−Cl1	2.5347(4)	2.3085(3)	2.4637(4)	2.3804(16)	2.2113(5)	2.2966(4)
M−Cl2	2.5573(4)		2.4721(4)	2.3908(14)		2.3275(4)
		angles				
N(1)−M(1)−N(2)	71.86(5)	71.75(3)	73.30(5)	80.05(15)	82.70(6)	77.13(5)
N(1)−M(1)−N(3)	72.43(5)		73.92(5)	80.12(15)	82.27(6)	76.40(5)
N(2)−M(1)−O(1)	73.15(4)	73.28(4)	72.58(4)	69.1(1)	75.20(6)	
O(2)−M(1)−N(3)	73.15(4)		72.60(4)	71.7(1)		
O(2), O(1)[a]−M(1)−O(1)	70.96(4)	70.15(5)	68.94(4)	61.3(1)		
N(1)−M(1)−Cl(1)	90.74(3)	93.697(10)	91.33(4)	94.95(11)	169.89(5)	159.71(4)
O(2), O(1)[a]−M(1)−Cl(1)	95.53(3)	88.68(3)	93.58(3)	92.61(9)		
N(3), N(2)[a]−M(1)−Cl(1)	88.89(4)	89.58(3)	88.97(4)	88.00(10)	98.20(4)	100.48(4)
N(2)−M(1)−Cl(1)	94.10(4)	92.74(3)	94.17(4)	93.19(11)	97.26(5)	99.13(4)
O(1)−M(1)−Cl(1)	84.30(3)	85.27(3)	83.67(3)	79.59(8)	107.12(3)	
N(1)−M(1)−Cl(2)	90.87(3)		92.60(4)	92.00(11)		98.01(4)
O(2)−M(1)−Cl(2)	83.10(3)		83.21(3)	81.56(9)		
N(3)−M(1)−Cl(2)	91.52(3)		92.21(4)	93.76(10)		94.62(4)
N(2)−M(1)−Cl(2)	86.47(3)		86.87(4)	87.44(10)		103.68(4)
O(1)−M(1)−Cl(2)	94.43(3)		93.04(3)	94.17(9)		
Cl(1)−M(1)−Cl(2)	178.388(16)	172.60(2)	176.070(15)	173.02(6)		102.234(16)
		dihedral angles—macrocyclic conformation				
N1−C5−C6−N2	25.0(2)	(N1−C3−C6−N2) 32.5(2)	24.8(2)	24.4(5)	−24.4(2)	−21.4(2)
N2−C7−C8−O1	−60.4 (2)	−56.6(2)	−58.6(2)	−63.0(5)	66.2(2)	72.7(2)
O1−C9−C10−O2	59.5(2)	(O1−C9−C9−O1) 55.8(2)	58.1(2)	56.5(5)	−65.8(2)	−66.8(2)
O2−C11−C12−N3	−59.8(2)	(O1−C8−C7−N2) −56.6(2)	−57.8(2)	−59.7(4)	64.8(2)	64.7(2)
N3−C13−C1−N1	32.5(2)	(N2−C6−C3−N1) 27.7(2)	29.8(2)	20.7(5)	−4.7(2)	−3.3(2)

[a]Symmetry code for **3**·2CH_3OH: $-x + 1, y, -z + 3/2$.

times higher. The difference in the donor atom arrangement around the central metal atom could be explained by higher oxidation state of iron atom, which has smaller ionic radius resulting in shorter and stronger bonds forcing the more rigid and thus more planar arrangement. The better planarity of the ligand-donor atoms is, on the other hand, compensated by larger twisting of the ethylene and benzylene bridges, which is apparent from the deviation of the benzyl carbon atoms (C6 and C13) under and above this plane: 0.55 Å for **1**, 0.74 Å for **2**, 0.56 and 0.55 Å for **3**. The obtained deviation values can be compared only in the case of Mn(II) with the value for complex with the corresponding Schiff base [Mn(15-pydienN_3O_2)Cl_2]·H_2O[16] (0.049 Å), which illustrates much higher flexibility of the macrocyclic scaffold of **L** in comparison with more rigid 15-pydienN_3O_2, but in general, good planar location of these six atoms. The coordination environment of Mn(II) in [Mn(15-pydienN_3O_2)Cl_2]·H_2O[16] is very similar and differs only in shorter Mn−N(imine) distances (~2.25 Å).

The molecular structure of Mn(II) complex is very similar to the previously determined structure of [Mn(**L**)Cl_2][Mn(**L**)-(H_2O)Cl]Cl·1.5H_2O[22] in which the same structural unit [Mn(**L**)Cl_2] was found. The length of Mn−N(pyridine) bond was found to be nearly identical to that determined for **2**·2H_2O, that is, 2.218 Å, and all the other bonds differed only negligibly. Crystal structures of other Mn(II) complexes [Mn(15-pydienN_3O_2)$(NCS)_2$],[2] [Mn(15-pydienN_3O_2)(H_2O)-Cl]ClO_4·CH_3OH,[14] [Mn(15-pydienN_5)(H_2O)$_2$]·4H_2O,[60] Mn-(15-pydienN_5)(H_2O)$_2$]·Cl(ClO_4),[61] and [Mn(15-pydienN_5)-Cl_2]·H_2O[16] were previously described as well (for the structural formulas of the ligands, see Figure 1).

Complexes of **L** with other transition metals, except for Mn(II), have not been reported yet; thus, there is no crystal structure of structurally similar Fe(III) complex, despite few Fe(III) complexes prepared with 15-pydienN_3O_2 and chlorido coligands.[2] In CSD, there are deposited some X-ray structures of Fe(III) complexes with different ligands, for example, [Fe_2(15-pydienN_5)$_2$($OH)_2O$](ClO_4)$_4$,[62] [Fe(15-pydienN_5)-$(NCS)_2$]ClO_4,[62,63] or some Fe(II) complexes, namely, [Fe-(15-pydienN_3O_2)$(CN)_2$]·H_2O,[8] ([(Fe(15-pydienN_3O_2)-(H_2O))$_2$Cr$(CN)_6$](ClO_4)·3H_2O,[18] [Fe(15-pydionN_5)-$(CH_3OH)_2$]·CH_3OH,[32] or [Fe(15-pydienN_5)(H_2O)$_2$]·Cl(ClO_4).[64] The total number of previously described Co(II)/(III) complexes of different 15-membered pyridine-based macrocycles is much lower than in the case of Mn(II) or Fe(III)/Fe(II). The crystal structures deposited with the CSD are as follows: [(Co(15-pydienN_3O_2))$_2$Cr$(CN)_6$]ClO_4·8H_2O[17] with CN of 7 for Co(II) and [Co(15-pyN_5-Me_2)Cl](ClO_4)$_2$[65] in which CN of Co(III) is only 6.

Noncovalent contacts, especially hydrogen bonds and $\pi-\pi$ stacking, play a crucial role in the final crystal packing of **1**−**3**. The crystal structures of **1**·2CH_3OH and **3**·2CH_3OH are very similar, and both are stabilized by intermolecular hydrogen bond network. The [M(**L**)Cl_2] units are connected together through the N−H···Cl hydrogen bonds into a zigzag 1D chain, while two CH_3OH crystal solvent molecules are linked to the [M(**L**)Cl_2] unit via O−H···Cl hydrogen bonds (Figure 3b,

DOI: 10.1021/ic503054m
Inorg. Chem. 2015, 54, 3352−3369

Table 3. Selected Hydrogen Bond Parameters (Å, deg) for Complexes 1−6

D−H···A[a]	d(D−H)	d(H···A)	d(D···A)	∠(DHA)	D−H···A	d(D−H)	d(H···A)	d(D···A)	∠(DHA)
1·2CH_3OH					**4**				
N(2)−H(2N)···Cl(1)[b]	0.93	2.74	3.5555(14)	146	N(2)−H(2N)···Cl(2)[c]	0.75(5)	2.69(4)	3.305(4)	142
N(3)−H(3N)···Cl(2)[d]	0.93	2.50	3.3415(14)	151	N(3)−H(3N)···Cl(1)[e]	0.92(5)	2.55(5)	3.290(4)	138
O(3)−H(3V)···Cl(1)	0.84	2.31	3.1302(15)	166	C(3)−H(3A)···Cl(1)[f]	0.95	2.8058(16)	3.511(5)	132
O(4)−H(4W)···Cl(2)	0.84	2.34	3.1538(15)	164	C(4)−H(4A)···Cl(2)[g]	0.95	2.8490(23)	3.630(5)	140
C(3)−H(3A)···Cl(1)[h]	0.95	2.8269(4)	3.5276(17)	131	C(3)−H(3A)···O(1)[f]	0.95	2.504(3)	3.289(6)	140
C(3)−H(3A)···Cl(2)[i]	0.95	2.9172(5)	3.6770(18)	138					
2·2H_2O					**5**				
N(2)−H(2N)···O(2)	0.854(18)	2.105(18)	2.8905(17)	153	N(3)−H(3N)···Cl(2)	0.87(2)	2.29(2)	3.1170(17)	158
O(2)−H(2V)···Cl(2)	0.822(18)	2.375(19)	3.1951(12)	176	N(2)−H(2N)···Cl(2)[j]	0.89(2)	2.39(2)	3.2140(17)	155
O(2)−H(2W)···Cl(2)[k]	0.80(2)	2.40(2)	3.1971(13)	174	C(2)−H(2A)···Cl(1)[l]	0.95	2.7499(5)	3.476(2)	134
C(1)−H(1A)···Cl(1)[m]	0.94(3)	2.86(2)	3.4886(15)	125	C(3)−H(3A)···Cl(2)[n]	0.95	2.7966(5)	3.595(2)	142
3·2CH_3OH					**6**				
O(3) −H(3W)···Cl(1)	0.79	2.35	3.1344(15)	172	N(2)−H(2N)···Cl(2)[o]	0.929(1)	2.5474(4)	3.3254(13)	141
O(4) −H(4W)···Cl(2)	0.95	2.21	3.1514(16)	170	C(3)−H(3A)···Cl(2)[p]	0.95	2.7446(4)	3.5024(15)	137
N(2) −H(2N)···Cl(1)[q]	0.871(19)	2.843(19)	3.5929(15)	145	C(4)−H(4A)···Cl(2)[r]	0.95	2.7728(4)	3.7028(18)	166
N(3) −H(3N)···Cl(2)[s]	0.842(19)	2.597(19)	3.3675(15)	153					
C(3)−H(3A)···Cl(1)[t]	0.95	2.8284(4)	3.5376(16)	132					
C(3)−H(3A)···Cl(2)[u]	0.95	2.9289(4)	3.6930(18)	138					

[a]Symmetry transformations used to generate equivalent atoms: [b]$x - 1/2, -y + 3/2, z - 1/2$. [c]$-x, -y + 1, -z + 1$. [d]$x + 1/2, -y + 3/2, z + 1/2$. [e]$-x + 1, -y + 1, -z + 1$. [f]$x, -y + 3/2, z + 1/2$. [g]$x, y + 1, z$. [h]$-x + 3/2, y + 1/2, -z + 3/2$. [i]$-x + 1, -y + 2, -z + 1$. [j]$-x + 1, -y, -z + 1$. [k]$-x, -y, -z + 1$. [l]$x, y + 1, z$. [m]$-x, -y + 1, -z$. [n]$-x + 1, -y + 1, -z + 1$. [o]$-x + 2, -y + 1, -z$. [p]$-x + 1, -y, -z$. [q]$x + 1/2, -y + 1/2, z + 1/2$. [r]$x - 1, y, z$. [s]$x - 1/2, -y + 1/2, z - 1/2$. [t]$-x + 1/2, y + 1/2, -z + 1/2$. [u]$-x + 1, -y + 1, -z + 1$.

Supporting Information, Figure S3b, and Table 3). The two neighboring infinite chains are connected by face-to-face $\pi-\pi$ stacking interactions between two pyridine rings of two $[M(\mathbf{L})Cl_2]$ units (the centroid···centroid distance = Cg···Cg = 3.5658(1) Å for **1**, Cg···Cg = 3.5834(2)Å for **3**), and the crystal structure is further stabilized by bifurcated C3−H3A···Cl1(Cl2) noncovalent contact (with the C···Cl distances of 3.528(2) and 3.677(2) for **1**, 3.538(2) and 3.693(2) for **3**, respectively) resulting in a separated 2D sheet without any noncovalent contacts between each other (Figure 3c and Supporting Information, Figure S3c).

In the case of **2**, one positive charge of the complex $[Fe(\mathbf{L})Cl_2]^+$ cation is compensated by one uncoordinated chloride counterion, which is together with the crystal water molecules involved in an extensive system of intermolecular hydrogen bonds (Table 3).

It is clearly shown in Figure 4b that the crystal water molecules and uncoordinated chloride ions form 1D chain mediated by $O-H_{water}\cdots Cl_{uncoordinated}$ hydrogen bonds, and the macrocyclic units $[Fe(\mathbf{L})Cl_2]^+$ form second 1D chain mediated by weak $\pi-\pi$ interactions (Cg···Cg = 4.5205(1) Å) and $C-H_{aromatic}\cdots Cl$ contacts. These two chains are connected to each other by a strong $N-H\cdots O_{water}$ hydrogen bond (N···O = 2.891(2) Å), and they alternate in the crystal structure as shown in Figure 4c.

Ni(II) Complex (4). The molecular structure of **4** is shown in Figure 5a, and selected interatomic distances and angles are given in Table 2. The coordination sphere of Ni(II) differs from the above-described complexes, because Ni(II) reveals a markedly distorted pentagonal bipyramidal geometry. Its CN could be classified as 5 + 2, because the Ni−N (1.987(4)−2.132(3) Å) and Ni−Cl distances (2.380(2) and 2.391(2) Å) are shortened in comparison with the above-described structures of complexes **1**−**3**, while the Ni−O distances are much more elongated (2.506(3) and 2.663(3) Å) indicating strong decrease in stability of Ni−O coordination bonds, because the mean value of the Ni−O bond distance is only 2.055 Å, and 90% of all the observed Ni−O bonds, as found in CSD, have length in the range of 1.964−2.144 Å. Nevertheless, there are some examples of Ni(II) complexes in which the Ni−O distance is close to or exceeds 2.50 Å.[33]

Additionally, Ni(II) atom and both chloride atoms are disordered between two positions with the occupancy factors of 0.876(7) and 0.124(7). (Note: atoms with higher occupancy factors were taken into account in connection with the above-described interatomic parameter evaluations.) The mean deviation value from the NiN_3O_2 least-squares plane is 0.17 Å illustrating the worst planar location of these atoms in comparison with the all three above-described complexes. The most deviated atoms from this plane are surprisingly aliphatic carbon atoms C7 and C12 (0.39 Å) together with the benzyl carbon atoms C6 and C13 (0.37 and 0.38 Å).

In the crystal structure of **4**, there are N−H···Cl hydrogen bonds, whose presence results in the formation of 1D chainlike structure depicted in Figure 5b.

These chains are connected to each other by additional bifurcated C3−H3A···O1(Cl1) (with C···O and C···Cl distances of 3.289(6) and 3.511(5)) and $C-H_{aromatic}\cdots Cl$ noncovalent contacts, and thus, these chains form two alternating layers with parallel arrangement of these chains, which are rotated by 78° in these two layers (Figure 5c, Table 3). Moreover, there is no evidence for any $\pi-\pi$ interactions between any pyridine rings in the crystal structure. Surprisingly, there is no Ni(II) complex of 15-membered pyridine-containing macrocycle deposited in the CSD although several Ni(II) complexes of different 15-membered pyridine-based macrocycles have been previously prepared.[66,67]

Cu(II) and Zn(II) Complexes (5 and 6). The molecular structures of **5** and **6** are depicted in Figure 6a,b, respectively. In these two cases, drastic change in the coordination environment of the central metal atom occurs, and the macrocyclic ligand is markedly folded. All Cu−N bond lengths are the shortest from all the metal−nitrogen distances within the studied complexes; Cu−N(pyridine) is the shortest one

DOI: 10.1021/ic503054m
Inorg. Chem. 2015, 54, 3352−3369

(1.925(2) Å), while the other two Cu−N(aliphatic) bonds have the length of ∼2.03 Å. All these distances are ∼0.02 Å longer in **6**. The Cu−O distances are much more elongated, one distance is 2.721(2) Å, resulting in a weak semicoordination bond (Jahn−Teller effect), usually found for coordination of water, perchlorato and nitrato ligands or special carboxylates/sulfonates in Cu(II) complexes (CSD),[1] and the second distance is 3.816(2) Å, which clearly demonstrates that this second oxygen atom is not coordinated to Cu(II). The Zn−O distances are longer than 3 Å (3.113(2) and 4.030(2) Å), which indicates no coordination of these atoms to Zn(II). According to these facts, Cu(II) and Zn(II) adopt distorted square pyramidal geometry with CN 4 + 1 and 5, and the N_3OCl and N_3Cl_2 donor atom set, respectively. The calculated value of Addison's τ parameter helped us to describe the coordination geometry more precisely and to distinguish between the square pyramidal and trigonal bipyramidal arrangement.[68] The values were determined to be 0.09 for **5** and 0.17 for **6**, which suggest the square pyramidal geometry for each complex. In accordance with this fact, Cu(II) or Zn(II) atom is located only 0.06 or 0.30 Å above the MN_3Cl least-squares plane.

Similarly to that of **4**, the structures of **5** and **6** do not contain any solvent molecules; nevertheless, chloride counterions or chlorido ligands play an important role in the formation of hydrogen bonds network (Figure 6c,d and Table 3). Four N−H···$Cl_{(counterion)}$ hydrogen bonds connect two macrocyclic units $[Cu(\mathbf{L})Cl]^+$ into a pseudodimer (similarly two N−H···$Cl_{(coordinated)}$ hydrogen bonds connect two neutral $[Zn(\mathbf{L})Cl_2]$ units), and these dimers are additionally coupled via $\pi-\pi$ interaction between the pyridine rings (Cg···Cg = 3.8377(1) Å for **5** and Cg···Cg = 3.9266(1) Å for **6**) and via C−$H_{aromatic}$···Cl noncovalent contact(s) into a 1D chainlike structure (Figure 6c,d). The crystal structures of the following Cu(II) complexes with penta-aza macrocyclic ligands have been published to date: $[Cu(15\text{-}pyN_5)](PF_6)_2$[69] and $[Cu(15\text{-}pyN_5\text{-}Me_2)](PF_6)_2$,[65] in which Cu(II) has CN of 5, while the crystal structures of similar Zn(II) complexes were determined only for $[Zn(15\text{-}pydienN_5)(SCN)_2]\cdot C_2H_4Cl_2$[70] and $[Zn(15\text{-}pyN_5\text{-}Me_4)](ClO_4)_2$[67] with CN of 7 and 5 for Zn(II), respectively.

Comparison of the Crystal Structures of Complexes 1−6. Several trends can be observed when all the determined crystal structures of the studied complexes are compared. The metal−donor atom distances depend on the complexated metal atom, and their variations are displayed in Figure 7. When the central metal atom is changing from Mn(II) to Cu(II), the metal−nitrogen distances are shortening, while they are a little bit elongated going from Cu(II) to Zn(II). On the other hand, the metal−oxygen distances are elongating within the whole series going from Mn(II) to Zn(II). A consequence of these differences in metal−oxygen and metal-nitrogen distances is the shifting of the metal from the center of the cavity of the macrocyclic ligand closer to its part containing nitrogen atoms. This trend is also illustrated by the value of O−M−O angle (Table 2), which decreases, depending on the metal atom, from Mn(II) to Ni(II) (from complex **1** to **4**). The above-mentioned changes could be related to the changing ionic radius of the complexed metal ion (Table 4),[71] and the observed trend is in good correlation with the Irving−William series. Furthermore, it was published recently that the Jahn−Teller effect operating in Ni(II) complexes with CN of 7 could be another reason for the increase of the metal−oxygen distances.[72] Changing the metal from Mn(II) to Zn(II) (complex **1** to **6**), the macrocyclic cavity becomes too large for smaller cations, which results in a

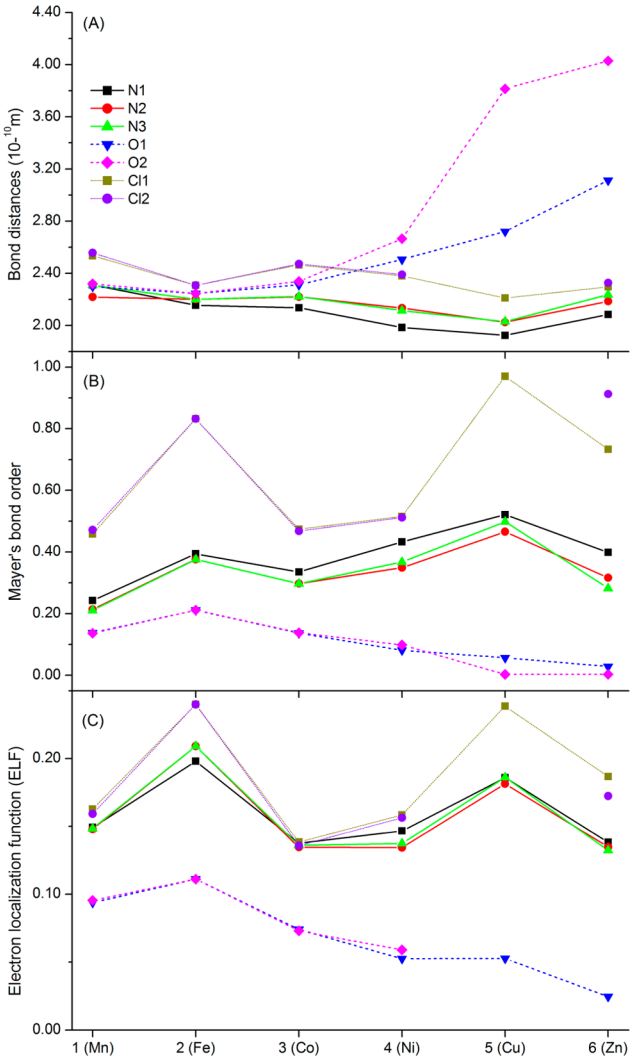

Figure 7. Variation of the metal−donor atom distances (A), Mayer's bond order (B), and electron localization function (C) in the studied complexes depending on the central metal atom.

folding of the macrocycle and reduction of the coordination number from 7 to 5. Mn(II), Fe(III), and Co(II) complexes **1**−**3** reveal CN of 7 with the $N_3O_2Cl_2$ donor atom set; Ni(II) complex **4** is somewhere between this transformation with two semicoordinated oxygen atoms (CN 5 + 2, $N_3O_2Cl_2$ donor atom set) as well as Cu(II) complex **5** with CN 4 + 1 and one semicoordinated oxygen atom (N_3OCl donor atom set). CN of 5 was found in the last-in-row Zn(II) complex **6** with the N_3Cl_2 donor atom set.

To support our conclusions, the molecular structures of complexes **4**−**6** were analyzed by program Shape 2.1 providing continuous shape measures.[73] Any coordination sphere can be described by an ideal polyhedron that has the lowest deviation from the real geometry. Thus, the lowest value of deviation for **4** was found for pentagonal bipyramid (from all possible polyhedra for CN = 5, 6, and 7, Supporting Information, Table S1), square for **5**, and square pyramid for **6** (all possible polyhedra for CN = 4, 5, and 6, Table S1). Except for **5**, the calculated results are in agreement with our previous presumption; nevertheless, low values of deviations were observed also for tetragonal pyramid or octahedron for **5** or **6**, respectively. Therefore, additional ab initio calculations

DOI: 10.1021/ic503054m
Inorg. Chem. 2015, 54, 3352−3369

Table 4. Dihedral Angles between Planes 1−3[a] Together with Donor Atom Deviations and Mean Deviation from the Least-Square Plane Defined by the Ligand Donor Atoms and the Central Metal Atom

complex	1·2CH$_3$OH	2·2H$_2$O	3·2CH$_3$OH	4	5	6
			dihedral angle (deg)			
plane1/plane2[a]	12.86	19.86	12.98	7.02	11.73	10.33
plane1/plane3[a]	77.71	70.53	77.10	82.81	85.89	85.95
plane2/plane3[a]	89.36	89.61	89.59	88.68	77.63	85.47
			deviation from the least-squares plane[b] (Å)			
metal	0.024	0.000	0.012	0.000	0.057	0.302
N1(py)	0.024	0.000	0.031	0.005	0.144	0.073
N2	0.155	0.047	0.146	0.151	0.095	0.068
N3	0.101	0.047[c]	0.088	0.167	0.095	0.067
O1/Cl1[b]	0.215	0.076	0.198	0.251	0.102	0.093
O2	0.209	0.076[c]	0.184	0.262		
mean	0.141	0.049	0.129	0.167	0.109	0.075
	Mn(II)	Fe(III)	Co(II)	Ni(II)	Cu(II)	Zn(II)
r_{ion}, Å[d]	0.83 (6)	0.645 (6)	0.745 (6)	0.69 (6)	0.73 (6)	0.74 (6)
	0.90 (7)			0.63 (5)	0.65 (5)	0.68 (5)

[a]Plane 1 defined by pyridine ring, plane 2 defined by donor atom set (N_3O_2, N_3 for **5** and **6**), plane 3 defined by Cl−M−Cl bond (Cl−Cu−O1 bond for **5**). [b]For **1**−**4** the least-squares plane defined by MN_3O_2, for **5** and **6** by MN_3Cl atoms. [c]In **2** only N2 and O1 are present. [d]r_{ion} = ionic radius for the ions in HS state, the value in parentheses stands for coordination number, ref 71.

concerning the strength of coordination bonds and coordination geometries were performed and are discussed later.

In accordance with this finding is the progress of the values of atom deviations and mean deviation from the least-squares plane MN_3O_2 listed in Table 4. This deviation is the lowest for Fe(III) (0.049 Å) and increases for Co(II) and Mn(II) (0.129, and 0.141 Å, respectively) to finally reach the largest value for Ni(II) (0.167 Å). The observed trend in the deviations can be related not only to the changes in the ionic radius of the complexated metal ions but also to a different charge of the ions and a different overall symmetry of the coordination spheres. When Fe(III) and Ni(II) complexes **2** and **4** are compared, the ionic radii of the ions are similar (Table 4), but Fe(III) has a larger change than the other ions providing stronger electrostatic attraction between the ion and ligand and thus has the most symmetrical coordination sphere of the series (the difference between the maximal and minimal metal−ligand donor atom distances is only 0.16 Å). On the other hand, Ni(II) complex **4** has lower charge and the most unsymmetrical coordination sphere in the series, related to the expected Jahn−Teller effect (the difference in metal−ligand donor atom distances is even 0.67 Å). The two oxygen atoms in **4** are only semicoordinated and thus have the largest deviation from the least-squares plane MN_3O_2. It could be also suggested that, for smaller cations, the donor atoms need to be closer to the metal, which could be accomplished by increased folding (rotation) of the macrocylic scaffold. Other parameters describing the geometric properties of the complex molecules are dihedral angles between three planes 1−3 listed in Table 4 (planes defined by (i) pyridine unit, (ii) nitrogen-oxygen donor atom set, (iii) Cl−M−Cl or Cl−Cu−O1 bonds). The plane2/plane3 dihedral angles are close to 90°, indicating almost perpedicular coordination of both chlorido ligands (no side-deformation of pentagonal bipyramid in axial position), except for **5**, in which the lower value of the angle indicates side-deformation of the apex of the tetragonal pyramid, which is in accordance with the low value of N2−Cu−O1 angle (75.20°). The plane1/plane3 dihedral angles are in the range of 70−85°, which illustrates that the pyridine ring is not perpedicular to Cl−M−Cl or Cl−Cu−O1 vectors but is turned by 15−30°, and the highest value was found in **2**, while the lowest value was found in **6**. This twisting of pyridine ring to Cl−M−Cl(O1) vectors as well as to nitrogen−oxygen donor atom set is documented by values of plane1/plane2 dihedral angles. The highest torsion was found in **2** (corresponding to the highest deviation of C6 benzyl atoms from the plane formed by central metal and all donor atoms) and the lowest value in **4**. This is in correlation with the mean deviation from the plane defined by all donor atoms and central metal atom, which has an opposite trend. This finding confirmed our presumption that the planar arrangement of the five donor atoms of the macrocycle around the metal center results in a big torsion of all other bonds in terms of higher deviation of the whole macrocycle scaffold from the planarity. This trend can be also illustrated by the values of dihedral angles listed in Table 2.

Concerning the noncovalent contacts, important intermolecular hydrogen bonds network was found in each crystal structure. The most important hydrogen bonds were N−H···O, O−H···Cl, and N−H···Cl with donor···acceptor distances ranging from ∼3.1 to ∼3.6 Å indicating their weak bonding character. Only one strong hydrogen bond N−H···O_{water} (N···O distance 2.89 Å) was found in **2**. The complex units were usually connected together via these hydrogen bonds or weak C−H···Cl (C···Cl distances from ∼3.5 to ∼3.7 Å) or C−H···O (C···O distance 3.289(6) Å) hydrogen bonds as well as via $\pi-\pi$ interaction between the pyridine rings (not found in **4**) always in slipped (offset) face-to-face alignment (Cg···Cg from ∼3.6 to ∼4.5 Å), which significantly contribute to the final 3D crystal packing. Finally the metal···metal distances in each complex were investigated, and the value of the shortest distance in each structure increases going from Cu(II) to Fe(III); it later drops for Mn(II) (see later in magnetic measurements section). In context of involved noncovalent contacts, the shortest metal··· metal distances were found for complex units connected with hydrogen bonds (**1**, **3**, **4**, and **5**) or other noncovalent contacts (**2**). Thus, these noncovalent contacts play an important role in additional investigation of magnetic properties of these compounds (vide infra).

Ab Initio Calculations. Nowadays, there are many properties that can be thoroughly studied by ab initio

DOI: 10.1021/ic503054m
Inorg. Chem. 2015, 54, 3352−3369

Table 5. Comparison of Selected ZFS Parameters and *g*-Factors Determined for Complexes 1−5 Together with the Results of Magnetic Analysis Using Different Models of the Spin Hamiltonian

compound	1	2	3	4	5
complexed metal	Mn(II)	Fe(III)	Co(II)	Ni(II)	Cu(II)
electron configuration	$3d^5$	$3d^5$	$3d^7$	$3d^8$	$3d^9$
spin state S	5/2	5/2	3/2	1	1/2
ZFS values based on CASSCF/NEVPT2 calculations					
D (cm^{-1})	0.0171	−0.394	45.0	−6.08	
E/D	0.112	0.235	0.0433	0.245	
g_1	2.000	2.000	2.004	2.218	2.068
g_2	2.000	2.000	2.421	2.239	2.071
g_3	2.000	2.000	2.465	2.275	2.349
The largest isotropic exchange J values based on DFT calculations					
J^Y (cm^{-1})	−0.11	−0.11	−0.02	−0.52	−2.49
d(M···M) (Å)	6.6268(4)	7.5084(2)	8.6291(4)	6.528(2)	9.6921(4)
Magnetic analysis with the Curie−Weiss law[a]					
g	2.04	2.10	2.48	2.28	2.07
Θ (K)	−0.05	−3.1	−9.5	−1.6	−3.5
Magnetic analysis with a monomeric model[b,c]					
g	2.05	2.05	g_{xy} = 2.48	2.27	
D (cm^{-1})			40.0	−5.13	
E/D				0.33	
zj (cm^{-1})	−0.11	−0.35	−0.045	−0.84	
χ_{TIM} (1×10^{-9} m^3 mol^{-1})		9.5	10.0		
Magnetic analysis with a dimeric model[b]					
J (cm^{-1})	−0.093	−0.27	−0.028	−0.75	−3.39
g	2.05	2.05	g_{xy} = 2.48	2.27	2.03
D (cm^{-1})			40.2	−6.78	
E/D				0.12	
χ_{TIM} (1×10^{-9} m^3 mol^{-1})		9.5	10.0		0.50
Magnetic analysis with a 1D chain model[b]					
J (cm^{-1})	−0.051	−0.16	−0.018	−0.48	−2.43
g	2.05	2.05	g_{xy} = 2.48	2.27	2.03
D (cm^{-1})			40.0	−6.02	
E/D				0.15	
χ_{TIM} (1×10^{-9} m^3 mol^{-1})		9.5	10.0		0.5

[a]Values for **3** (M = Co) were derived for susceptibility above 50 K. [b]In case of **3** (M = Co) g_z was fixed to 2.0. [c]Model was not applicable to **5** (M = Cu), estimated $zj < -5$ cm^{-1}.

theoretical methods, and in this work we used them with the aim (i) to evaluate the chemical bonding between metal atoms and ligand donor atoms within this series of compounds **1**−**6**, (ii) to evaluate the ZFS tensor parameters D and E, and (iii) to evaluate the intermolecular magnetic interactions. In all these calculations, the relativistic effects were included with the help of the scalar relativistic contracted version of def2-TZVP(-f) basis functions and with zero order regular approximation (ZORA) using ORCA computational software (see details in Experimental Section).

From the discussion related to X-ray structures of **1**−**6** follows that the CN varies between 4 + 1 and 7 within the reported series of compounds, and there are some cases in which the assignment based on bond length only is ambiguous. Therefore, the strength of donor−acceptor bonds within all the coordination chromophores in complexes **1**−**6** was evaluated by DFT calculations using the well-established B3LYP functional. The single-point energy calculations (B3LYP +ZORA/def2-TZVP(-f)) were performed for neutral complex units $[M(\mathbf{L})Cl_2]$ (**1**, **3**, **4**, **6**) and complex cations of $[Fe(\mathbf{L})Cl_2]^+$ (in **2**) and $[Cu(\mathbf{L})Cl]^+$ (in **5**), and subsequently the geometry-basis-wave function (GBW) file was transformed to MOLDEN format and analyzed using the Multiwfn program.

To quantify donor−acceptor bonds within the complexes, the Mayer's bond analysis was the first choice, and the results are summarized in Figure 7b. According to this bond index, the strongest bonds were calculated between the central metal atoms (M) and chlorido ligands (M−Cl), medium strength bonds were between M and nitrogen atoms of the **L** ligand, and the weakest ones were found for the M−O bonds. In general, the pattern found in this plot copies the trend found for M−Cl/N/O bond lengths very well, which means the shorter bond length correlates with the higher Mayer's bond order. Furthermore, the bond order of the M−O bond type systematically decreases from iron to zinc metal centers, crossing to semicoordination (M−O1 for M = Cu) or lacking any bond at all (M−O1 for M = Zn and M−O2 for M = Cu, Zn).

Moreover, topological analysis was performed using the total molecular electronic density $\rho(r)$ and the Laplacian of $\rho(r)(\nabla^2\rho(r))$ based on atom in molecule (AIM) calculations. The so-called bond critical points of the type (3,−1) were located between M−Cl/N/O bonds, and in these points, the ELF was calculated to quantify these donor−acceptor bonds. The results are plotted in Figure 7c and essentially complement Mayer's bond analysis showing the same trends within the

DOI: 10.1021/ic503054m
Inorg. Chem. 2015, 54, 3352−3369

Table 6. Metal···Metal Distances Found in the Crystal Structures of Complexes 1−5 in Context of Noncovalent Contacts Accompanied by Results of DFT Calculations of Magnetic Exchange[a]

complex	1·2CH_3OH	2·2H_2O	3·2CH_3OH	4	5
hydrogen bonds	6.6268(4)		6.5656(6)	6.528(2)	4.2366(3)
Δ (cm^{-1})	[−1.346]		[−0.008]	[−1.046]	[−0.318]
J^R/J^Y (cm^{-1})	−0.09/−0.11		0.00/0.00	−0.35/−0.52	−0.32/−0.64
π−π interactions	8.7238(4)	8.5920(4)	8.6291(4)		
Δ (cm^{-1})	[−0.367]	[−0.499]	[−0.079]		
J^R/J^Y (cm^{-1})	−0.02/−0.03	−0.03/−0.04	−0.01/−0.02		
interchain	7.9151(4)	7.4859(2)	7.9998(4)	7.639(2)	7.3285(4)
Δ (cm^{-1})	[−0.173]	[−0.845]	[0.377]	[−0.627]	[+0.027]
J^R/J^Y (cm^{-1})	−0.01/−0.01	−0.06/−0.07	+0.06/+0.08	−0.21/−0.31	+0.03/+0.05
					9.6921(4)
		7.5084(2)			[−1.244]
		[−1.435]			−1.24/−2.49
		−0.10/−0.11			9.8135(4)
					[−0.072]
					−0.07/−0.14

[a]M···M distances in angstroms, [Δ] = $E_{BS} - E_{HS}$ in inverse centimeters, the isotropic exchange values J^R/J^Y in inverse centimeters rounded to two decimal places.

series. The M−Cl/N types of bonds are again the strongest ones, but now ELF values of M−Cl and M−N bonds are much closer than in Mayer's bond analysis. Again, ELF of M−O bonds decreases from iron to zinc, but in the case of M = Cu(II), Zn(II), the bond critical points of the type (3,−1) were not found between M and O2 atoms, simply confirming no coordination. Despite the absence of sharp drop in ELF values, we may conclude that the analysis showed that (i) Mn(II), Fe(III), and Co(II) atoms have CN 7 with the $N_3O_2Cl_2$ donor atom set, (ii) the Ni(II) has 5 + 2 coordination mode with the $N_3O_2Cl_2$ donor atom set, (iii) the Cu(II) has 4 + 1 coordination mode with the N_3OCl donor atom set, and (iv) the Zn(II) has 5 coordination mode with the N_3Cl_2 donor atom set with both the O atoms situated outside the inner coordination sphere despite the critical point of the type (3,−1) was found for Zn and O1 indicating ∼twofold weaker interaction in comparison with the O1 semicoordination in Ni(II) and Cu(II) complexes **4** and **5**.

Such various coordination modes and geometries found in this series have of course substantial impact also on magnetic properties of the ground state for the reported compounds **1**−**5** (M = Mn, Fe, Co, Ni, Cu). (Note: the Zn(II) complex **6** was excluded form magnetic study owing its diamagnetism.) This is why we employed the ab initio calculations of ZFS parameters based on state-averaged complete-active-space self-consistent field (SA-CASSCF) wave functions accompanied by N-electron valence second-order perturbation theory (NEVPT2). The active space of these CASSCF calculations was composed of the appropriate number of electrons according to metal atom in five metal-based d-orbitals. The dominant spin−orbit coupling contributions from excited states led to ZFS tensors and hence to the determination of axial and rhombic single-ion parameters D and E, respectively (Table 5). The contributions of the excited states to ZFS terms are summarized in Tables S2−S5 (see Supporting Information). The quasi-degenerate perturbation theory was used to extract information about ZFS, but also values calculated by second-order perturbation theory are listed for comparison in Table S6 (see Supporting Information).

The largest D-parameters were found in compound **3** (M = Co), D = 45.0 cm^{-1}, and in compound **4** (M = Ni), D = −6.08 cm^{-1}, while **1** and **2** have $|D|$ less than 1 cm^{-1}. The largest rhombicity was found for compound **4** (M = Ni), E/D = 0.245. The nature and magnitude of the magnetic anisotropy of Co(II) and Ni(II) complexes **3**, and **4**, respectively, is completely in accordance with the theoretical and experimental investigations of other heptacoordinated complexes of ligands **L3** and **L4**.[35] The origin of the large positive and negative D-values for Co(II), and Ni(II) complexes, respectively, is related to the different contribution of excited states to the ground state; for Co(II) complex all excited states contribute to a positive D-value, whereas for Ni(II) the contributions are opposite.[35] The axes of ZFS and g-tensors together with molecular structures are visualized in Supporting Information (Figure S4). In all cases, both g-tensor and ZFS-tensor axes coincide; only in the case of compound **1** (M = Mn) there is a little discrepancy, which however can also be related to a very small value of the ZFS tensor parameters, hence, to enhanced numerical noise in extracting ZFS orientation axes. In general, the main axes of ZFS tensors for M = Mn, Fe, Co, Ni are approximately located along the Cl−M−Cl, N2−M−N3, and N1−M bonds (Supporting Information, Figure S4). In the case of M = Cu, the two components of g-tensors lies in the CuN1N2N3Cl1 plane, almost along N2−Cu−N3 and N1−Cu−Cl1 bonds, and the last g-component is perpendicular to this plane. If the main magnetic axis is defined by D-tensor, then the g-axes for compounds **3** and **4** can be assigned as $g_x = g_2$ = 2.421, $g_y = g_3$ = 2.465, $g_z = g_1$ = 2.004 for **3** and $g_x = g_2$ = 2.239, $g_y = g_1$ =2.218, $g_z = g_3$ = 2.275 for **4** (Figure, S4, see Supporting Information).

The last topic to discuss before focusing on experimental magnetic properties of the reported compounds is the possibility that intermolecular interactions may lead to non-negligible magnetic exchange among mononuclear complexes in solid state. With the aim to estimate such magnetic interactions through noncovalent superexchange pathways (hydrogen bonds, π−π stacking), the isotropic exchange constants J were calculated for various dinuclear moieties using the BS state approach at the B3LYP+ZORA/def2-TZVP(-f) level of theory. Then, the spin Hamiltonian postulated for such dimer

$$\hat{H} = -J(\vec{S}_1 \cdot \vec{S}_2) \quad (1)$$

DOI: 10.1021/ic503054m
Inorg. Chem. 2015, 54, 3352−3369

and the energy difference Δ between the BS spin state and the HS state

$$\Delta = E_{BS} - E_{HS} \quad (2)$$

were used to calculate J-value either by the Ruiz's approach

$$J^{R} = 2\Delta/[(S_1 + S_2)(S_1 + S_2 + 1)] \quad (3)$$

or by a more general Yamaguchi's approach

$$J^{Y} = 2\Delta/[\langle S^2\rangle_{HS} - \langle S^2\rangle_{BS}] \quad (4)$$

in which also spin-expectation values of HS and BS states are used.

The outputs of these calculations are summarized in Table 6, in which Δ, J^{R}, and J^{Y} are listed for all the relevant dimers according to the X-ray discussion. The relevant molecular fragments are visualized in Figure S5 (Supporting Information). To compare the strength of magnetic exchange for systems with different spins ranging from $S_i = 1/2$ to $S_i = 5/2$, we must note that J-parameter is not the best one, because we would like to compare the overall splitting of S-levels resulting from the isotropic exchange, which means the energy difference between $S_{min} = |S_1 - S_2| = 0$ and $S_{max} = (S_1 + S_2)$ levels, which correlates with above-defined Δ from DFT calculations. The largest Δ values, $|\Delta| > 1$ cm^{-1}, were found (i) in a dinuclear fragment of **1** (d(Mn···Mn) = 6.6268(4)), where the N−H···Cl hydrogen bonds dominates, (ii) in a dinuclear fragment of **2** (d(Fe−Fe) = 7.5084(2)), where weak C−H···O and C−H···Cl noncovalent contacts are present, (iii) in a dinuclear fragment of **4** (d(Ni−Ni) = 6.528(2)), where N−H···Cl hydrogen bond exists, and (iv) in a dinuclear fragment of **5** (d(Cu−Cu) = 9.6921(4)), where C−H···Cl noncovalent contacts are found. The spin densities of the last case are depicted for BS spin state in Figure 8. The important output emerged from these calculations is

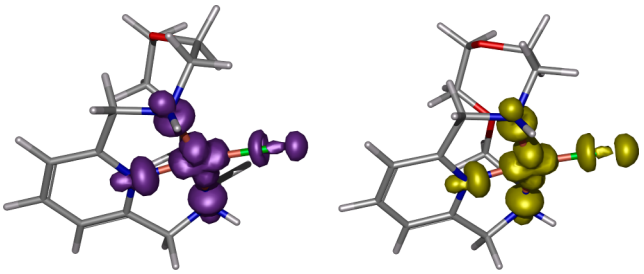

Figure 8. Calculated spin-density distribution using B3LYP+ZORA/def2-TZVP(-f) for $\{[Cu(\mathbf{L})Cl]_2\}^{2+}$ of **5** (Cu···Cu distance 9.6921(4) Å) for the BS state. Positive and negative spin densities are represented by violet and yellow surfaces, respectively. The isodensity surfaces are plotted with the cutoff values of 0.005 ea_0^{-3}.

that the strength of magnetic exchange cannot be solely judged by metal···metal distance and by type of noncovalent contacts. This is nicely demonstrated in the case of Cu(II) complex **5**, in which the strongest antiferromagnetic exchange was found for almost the largest Cu···Cu distance (Table 6). To summarize the J-values, the compounds in presented series can be sorted by increasing expected antiferromagnetic exchange as follows: **3** < **1** < **2** < **4** < **5**, which means minimal magnetic exchange J is estimated for compound **3** (M = Co) and the largest J for compound **5** (M = Cu).

Magnetic Properties. With the aim to extract the spin Hamiltonian parameters describing the magnetic anisotropy and eventually intermolecular magnetic exchange from experimental magnetization data, several models were applied. First, the mononuclear spin Hamiltonian (H^{mono}) with molecular field correction parameter was postulated

$$\hat{H}^{mono} = D(\hat{S}_z^{\,2} - \hat{S}^2/3) + E(\hat{S}_x^{\,2} - \hat{S}_y^{\,2}) + \mu_B B g \hat{S}_a - zj\langle\hat{S}_a\rangle\hat{S}_a \quad (4a)$$

where D and E are the single-ion axial and rhombic ZFS parameters, the next part is the Zeeman term, and the last component represented with the zj variable is the common molecular-field correction parameter, which is due to intermolecular interactions. The $\langle S_a\rangle$ is a thermal average of the molecular spin projection in a direction of magnetic field defined as $B_a = B(\sin(\theta)\cos(\varphi), \sin(\theta)\sin(\varphi), \cos(\theta))$ with the help of the polar coordinates. Then, the molar magnetization in a-direction of magnetic field can be numerically calculated as

$$M_a = -N_A \frac{\sum_i (\sum_k \sum_l C_{ik}^{+}(Z_a)_{kl} C_{li}) \exp(-\varepsilon_{a,i}/kT)}{\sum_i \exp(-\varepsilon_{a,i}/kT)} \quad (5)$$

where Z_a is the matrix element of the Zeeman term for the a-direction of the magnetic field, and C are the eigenvectors resulting from the diagonalization of the complete spin Hamiltonian matrix. The inclusion of zj means that iterative procedure must be applied.[37] Then, the averaged molar magnetization of the powder sample was calculated as integral (orientational) average

$$M_{mol} = 1/4\pi \int_0^{2\pi} \int_0^{\pi} M_a \sin\theta \, d\theta \, d\varphi \quad (6)$$

The second model used to interpret experimental data sets we based on the dinuclear spin Hamiltonian (H^{di})

$$\hat{H}^{di} = -J(\vec{S}_1 \cdot \vec{S}_2) + \sum_{i=1}^{2} D_i(\hat{S}_{i,z}^{\,2} - \hat{S}_i^{\,2}/3) + E_i(\hat{S}_{i,x}^{\,2} - \hat{S}_{i,y}^{\,2}) + \mu_B B g_i \hat{S}_{i,a} \quad (7)$$

where the first term describes the isotropic exchange between paramagnetic metal atoms with spin S_i, and the rest of terms were already explained.

The last model tries to mimic 1D uniformly coupled spin chain by finite-sized closed ring with following spin Hamiltonian (H^{1D})

$$\hat{H}^{1D} = -J(\vec{S}_1 \cdot \vec{S}_N) - \sum_{i=1}^{K-1} J(\vec{S}_i \cdot \vec{S}_{i+1}) + \sum_{i=1}^{K} D_i(\hat{S}_{i,z}^{\,2} - \hat{S}_i^{\,2}/3) + E_i(\hat{S}_{i,x}^{\,2} - \hat{S}_{i,y}^{\,2}) + \mu_B B g_i \hat{S}_{i,a} \quad (8)$$

In the case of the spin Hamiltonians H^{di} and H^{1D}, the molar magnetization in a-direction of magnetic field was calculated as

$$M_a = N_A kT \frac{d(\ln(Z))}{dB} \quad (9)$$

where Z is the partition function.

To provide the trustworthy parameters by magnetic analysis, both temperature- and field-dependent magnetization data were fitted simultaneously and are summarized in Table 5 for all the discussed models. In some cases, the temperature-independent magnetism correction χ_{TIM} was applied to describe the effect of either the contribution of excited electronic states, the so-called temperature-independent paramagnetism (χ_{TIP}), or the contribution of traces of magnetic impurities. The magnetic data for all the compounds **1**−**5** are depicted in Figure 9 for H^{1D}

DOI: 10.1021/ic503054m
Inorg. Chem. 2015, 54, 3352−3369

model, and the results for other two models can be found in Figure S6 (H^{mono}) and Figure S7 (H^{di}) in Supporting Information.

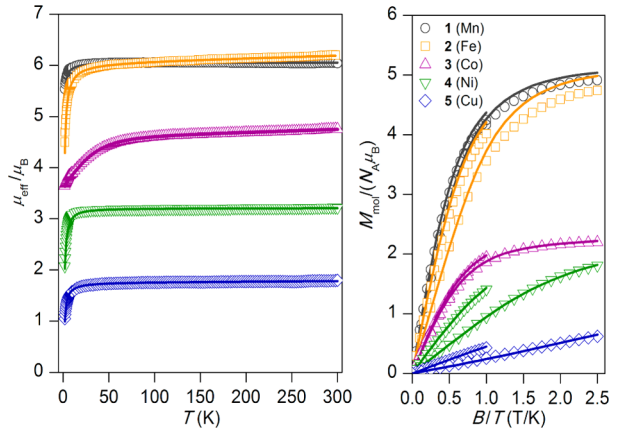

Figure 9. Magnetic data for compounds **1**−**5**. Temperature dependence of the effective magnetic moment (left) and the isothermal molar magnetizations measured at 2 and 5 K (right). The empty circles represent the experimental data points, and the full lines represent the best fits calculated by H^{1D} model (eq (8)) with parameters listed in Table 5. All data are scaled per one paramagnetic ion.

Mn(II) Complex (1). Temperature dependence of the effective magnetic moment for **1** is presented in Figure 9 together with the isothermal molar magnetization data measured at low temperature (2 and 5 K). The value of effective magnetic moment (μ_{eff}/μ_B) is 6.05 at room temperature, and is close to the spin-only value μ_{eff}/μ_B = 5.92 for the system with S = 5/2 and g = 2.0. A gradual decrease in μ_{eff}/μ_B is observed below 30 K, which can be attributed mainly to the presence of weak intermolecular noncovalent contacts in the solid state. The theoretical calculations predicted that the ZFS on the Mn(II) atom is very small, in a scale undetectable with magnetometry; thus, we simplified the spin Hamiltonian models and fitted experimental data with isotropic models (D = 0 and E = 0 were fixed). All applied models described experimental data in conformity with experimental data; g-parameter was equal to 2.05, which is expected value for $3d^5$ spin configuration. In case of H^{di}, the fitted J-value −0.093 cm^{-1} is very close to that derived by DFT (J^R/J^Y = −0.09/−0.11 cm^{-1}). However, when 1D chain model (H^{1D}) was applied with K = 7,[74] the smaller isotropic exchange was found (J = −0.051 cm^{-1}).

Fe(III) Complex (2). The magnetic data for **2** are essentially similar to those for **1** (Figure 9), but the effective magnetic moment is linearly decreasing from the room temperature value of 6.20 μ_B to the value of 5.87 μ_B at 50 K, which suggests the presence of a small amount of unknown magnetic impurity. Subsequent drop of μ_{eff}/μ_B to 4.49 μ_B at T = 1.9 K can be attributed to antiferromagnetic intermolecular interactions and eventually also to ZFS as evidenced by CASSCF/NEVPT2 calculations. We already demonstrated that in case of weak-exchange limit also the ZFS parameters of Fe(III) ion can be estimated from magnetic analysis;[75] however, in this case when the experimental data are affected by unknown magnetic impurity, we restricted spin Hamiltonians only to the isotropic case, and the effect of impurity was described by χ_{TIM}. The zj and J-values were found a little higher than those for analogous Mn(II) compound (Table 5) despite DFT J-values that were found similar for both systems, which possibly suggests that the neglecting of ZFS terms led to overestimation of the isotropic exchange. This is also supported by the fact that the calculated isothermal magnetization data at saturation limit are a bit higher than the experimental ones.

Co(II) Complex (3). The μ_{eff} adopts the value of 4.76 μ_B at room temperature, which is considerably higher than the spin-only value for S = 3/2 and g = 2.0 (μ_{eff}/μ_B = 3.87) owing to substantial contribution of the orbital angular momentum. When the material cooled, the μ_{eff}/μ_B continuously decreases to value of 3.65 at T = 1.9 K, which can be explained by a large ZFS and possibly also by intermolecular interactions. According to theoretical calculations, the large anisotropy of g-tensor is expected; thus, g_z was fixed to value of 2.0 and g_{xy} was left to be varied during the fitting procedure. Also, the theoretical rhombicity of this compound was found negligible, so the constraint E = 0 was set. In case of monomeric model H^{mono}, the zj value of −0.045 cm^{-1} is the smallest one within the reported series, and in the case of dimeric model H^{di}, the J-value is equal to −0.028 cm^{-1}, which is pretty close to the theoretical prediction (J^R/J^Y = −0.01/−0.02 cm^{-1}). The g_{xy} = 2.48 is also in good accordance with the calculated average of 2.44 from CASSCF/NEVPT2. The positive $D \approx 40$ cm^{-1} is close to calculated value of D = 45 cm^{-1}. The 1D chain model was applied for K = 5, which resulted in 1024 magnetic states. Because many matrix diagonalizations are needed in calculating powder average of magnetization, the spin permutational symmetry of the spin Hamiltonian was applied to construct new set of symmetry-adapted spin basis set using D_5 point group.[76] Such procedure split the total interaction matrix into submatrices A1 (N = 136), A2 (N = 72), E1 (N = 408), E2 (N = 408), labeled with the irreducible representations.[77] As a result, J = −0.018 cm^{-1}, g_{xy} = 2.48, and D = 40.1 cm^{-1} were found, all parameters close to H^{di} model and also to ab initio calculated parameters. Additionally, little lower positive D-values and values of g_{xy} were observed for other complexes of heptacoordinated Co(II) listed in Table 7.

Table 7. Comparison of Selected ZFS Parameters and g-Factors Determined for Previously Studied Complexes with Heptacoordinated Central Metal Ion

complex	D, cm^{-1}	E/D	g_{iso}	g_{xy}	ref
[Co(**L3**)(H_2O)(NO_3)](NO_3)	31	0	2.22		35
[Co(**L5**)](NO_3)$_2$·2CH_3CN	25		2.22		33
[Co(**L5**)](ClO_4)$_2$	26		2.15		33
[Co(**L6**)](ClO_4)$_2$	23.1			2.21	34
[Ni(**L3**)(H_2O)$_2$](NO_3)$_2$·2H_2O	−13.9	0.11	2.26		35
[Ni(**L4**) (NO_3)(CH_3OH)](NO_3)·CH_3OH	−12.5	0.10	2.22		36
[Ni(**L5**)](NO_3)$_2$·H_2O	15			2.27	33

Ni(II) Complex (4). The effective magnetic moment at room temperature, μ_{eff}/μ_B = 3.22, is significantly higher than the spin-only value for the system with S = 1 and g = 2.0 (μ_{eff}/μ_B = 2.83) for Ni(II) due to orbital momentum contributions. The abrupt decrease of its value at low temperature below 30 K is observed ending with 2.07 μ_B at T = 1.9 K in response to ZFS effect and intermolecular interactions. The mononuclear H^{mono} and dinuclear H^{di} confirmed important role of intermolecular interactions, zj = −0.84 cm^{-1} and J = −0.75 cm^{-1}, respectively, even indicating larger antiferromagnetic exchange than DFT

DOI: 10.1021/ic503054m
Inorg. Chem. 2015, 54, 3352−3369

calculations (J^R/J^Y = −0.35 cm^{-1}/−0.52 cm^{-1}). However, both models provided different values of rhombicity, E/D = 0.33 (D = −5.13 cm^{-1}) for H^{mono} model in contrast with E/D = 0.12 (D = −6.78 cm^{-1}) for H^{di} model. In case of the 1D chain model H^{1D}, the calculations were done for K = 5, and resulted in J = −0.48 cm^{-1}, D = −6.02 cm^{-1}, and E/D = 0.15. In all cases, the axial parameter D of ZFS was found close to value of −6.08 cm^{-1} derived from CASSCF/NEVPT2 procedure. In comparison with other complexes with heptacoordinated Ni(II), the obtained values of discussed parameters are in the same range (Table 7), but only the axial parameter D of ZFS is ∼2 times lower than for Ni(II) complexes of nonmacrocyclic Schiff bases **L3** and **L4**.

Cu(II) Complex (5). The last paramagnetic compound in this series is **5**, which shows magnetic behavior far from Curie-like behavior expected for an isolated mononuclear complex with S = 1/2 (Figure 9). The effective magnetic moment changes from 1.88 μ_B (T = 300 K) to 1.08 μ_B (T = 1.9 K) and also the isothermal magnetizations do not resemble Brillouin function. All these deviations from Curie behavior must be the outcome of intermolecular interactions, which is also supported by DFT calculations, where largest antiferromagnetic exchange was found to be J^R/J^Y = −1.24 cm^{-1}/−2.49 cm^{-1}. Furthermore, the H^{mono} model was not capable of describing this behavior (the iteration procedure failed for zj < −5 cm^{-1}). The dinuclear model H^{di} resulted in J = −3.39 cm^{-1}, while the application of H^{1D} model, with K = 19,[78] provided J = −2.43 cm^{-1}, which is close to Yamaguchi's isotropic exchange constant.

Bulk Magnetic Susceptibility Measurements. To compare the magnetic properties of complexes **1**−**5** in solid phase and in solution, the effective magnetic moment of each complex in D_2O or CD_3OD was calculated from the BMS measurement using Evans method.[79] Obtained results are in good agreement with the data in solid state, and thus no change or decomposition of studied complexes occurred upon dissolution in D_2O or CD_3OD (Table 8). The small differences between the effective magnetic moments in liquid and solid states could be related to the chlorido ligand substitution by water molecules in aqueous solution.

Table 8. Comparison of Effective Magnetic Moments[a] Obtained from SQUID Measurement in Solid State and BMS[b] Measurements in Solution

complex	1	2	3	4	5
μ_{eff}/μ_B (solid)	6.05	6.20	4.76	3.22	1.79
μ_{eff}/μ_B (in D_2O)	5.63	6.34	4.50	2.90	1.61
μ_{eff}/μ_B (in CD_3OD)	5.67	6.07	4.35	3.00	1.66

[a]Values are expressed in Bohr magnetons at 25 °C. [b]BMS = bulk magnetic susceptibility.

The stability of the solution samples was checked by measurement after one week, and no change in effective magnetic moment was observed except for **2** in water, for which the reduced μ_{eff} = 3.5 μ_B was found. This difference is in correlation with a drop of pD for solution of **2** from initial pD = 7.4 (same for all complex) to 2.3, which would suggest some complex decomposition resulting in precipitation of some hydroxo- or oxo-bridged species. Small drop of pD to 5.9 was observed for **5**; otherwise, the values of pD were constant for all other complexes.

Redox Properties. The redox properties of the complexes **1**−**6** were probed by cyclic voltammetry measurements. The cyclic voltammograms of Mn(II), Fe(III), and Cu(II) complexes **1**, **2**, and **5** in aqueous solution are depicted in Figure 10 and in MeCN in Figure 11; other complexes were in the measured range electrochemically silent. The obtained results are listed in Table 9. Quasi-reversible couple Mn(II)/Mn(III) was found at relatively high potential $E_{1/2}$ = 1.13 V with a large ΔE_p = 0.28 V in aqueous solution, which is in agreement with the previously published data for similar complex,[22] and at $E_{1/2}$ = 0.97 V (ΔE_p = 0.13 V) in MeCN. For **2**, a quasi-reversible couple Fe(II)/Fe(III) was found in water

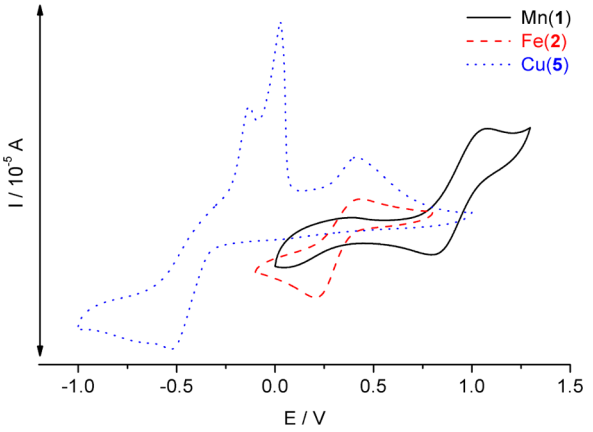

Figure 10. Cyclic voltammograms of 5 mM Mn(II) (**1**, black), Fe(III) (**2**, red), and Cu(II) (**5**, blue) complexes in 0.1 M KCl (glassy carbon working electrode, potential referred to Ag/AgCl reference electrode).

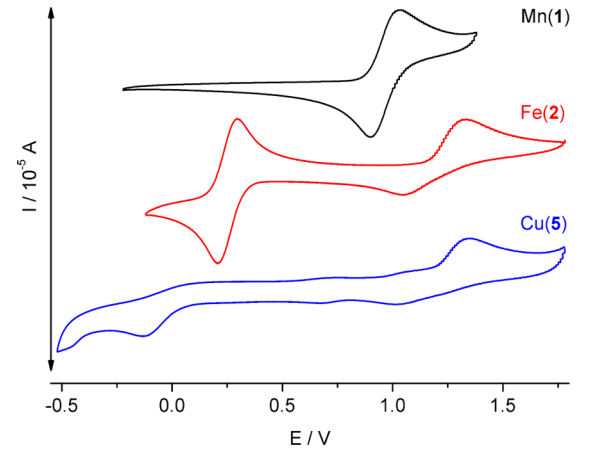

Figure 11. Cyclic voltammograms of 5 mM Mn(II) (**1**, black), Fe(III) (**2**, red), and Cu(II) (**5**, blue) complexes in 0.1 M TBAP in MeCN (glassy carbon working electrode, potential referred to SHE).

Table 9. Results of Cyclic Voltammetry Measurements

	water		MeCN	
complex	$E_{1/2}$[a]	ΔE_p[a]	$E_{1/2}$[a]	ΔE_p[a]
1	1133	285	967	129
2	514	221	248	81
5	E_{ox1} = 65 E_{ox2} = 223 E_{ox3} = 609	E_{red1} = −333	E_{red1} = −141	

[a]All potential values are given in millivolts for a scan rate of 0.1 V min^{-1}.

DOI: 10.1021/ic503054m
Inorg. Chem. 2015, 54, 3352−3369

($E_{1/2}$ = 0.51 V, ΔE_p = 0.22), whereas in MeCN this reduction wave became reversible ($E_{1/2}$ = 0.25 V, ΔE_p = 81 mV). This value of $E_{1/2}$ in MeCN is the same as that for [Fe(15-pydienN_3O_2)Cl_2]ClO_4 ($E_{1/2}$ = 0.25 V, ΔE_p = 110 or 60 mV)[2], which documents the same redox stability of Fe(III) complex of **L** and complex with corresponding Schiff base 15-pydienN_3O_2. In case of **5** in water, the cyclic voltammogram describes complex system with irreversible behavior providing three oxidation peaks (E_{ox1} = 0.06 V, E_{ox2} = 0.22 V, E_{ox3} = 0.61 V) and one reduction peak (E_{red} = −0.33 V). This peak at negative potential could be ascribed to the reduction of Cu(II) to Cu(I), which is shifted +0.4 V to positive potential in comparison with Cu(II) complex with analogous penta-aza-ligand [Cu(15-pyN_5)]$^+$.[69] The oxidation of Cu(I) complex is a multistep process, or probably some chemical reactions proceed on a Cu(I) complex, because the chlorido ligand can be substituted by water molecule (in all the complexes); thus, some hydroxo- or oxo- polynuclear complexes may be formed, and therefore their oxidation potentials differ significantly. There is only one irreversible reduction peak at E_{red} = −0.14 V for **5** in MeCN corresponding to the reduction of Cu(II) to Cu(I). The quality of the voltammogram is low due to the low solubility of **5** in MeCN, and the irreversibility of the Cu(II)/Cu(I) process could be mostly caused by insolubility of the Cu(I) product. Furthermore, the voltammograms of **2** and **5** in MeCN were accompanied by almost irreversible oxidation peak (E_{ox} = 1.33 V) together with low-intense reduction peak (E_{red} = 1.05 V) corresponding to the oxidation of chloride anions/reduction of chlorine, because free chloride counter-ions are presented in these two complexes, and therefore these peaks have much higher intensity than in case of the results for **1**.

In all the cases the peak potentials for observed couples in MeCN have lower values than in aqueous solution, which points to a more facile oxidation of Mn(II) or Fe(II) in MeCN than in water. The separation of the oxidation/reduction peaks was much lower in MeCN than in water. This behavior could be related to the substitution of the chlorido ligands in axial positions by solvent molecules, which is much more efficient in water than in MeCN and which could lead to a formation of differently substituted aqua-/hydroxo-/oxo- species (some chemical reactions can take place) in aqueous solution resulting in quasi-/irreversible behavior of the system.

CONCLUSIONS

In this work, new complexes of a pentadentate macrocyclic ligand **L** with Mn(II), Fe(III), Co(II), Ni(II), Cu(II), and Zn(II) (**1**−**6**) were prepared and thoroughly characterized. In the molecular structures of the first four complexes **1**−**4**, the metal atom is five-coordinated in a relatively planar macrocyclic cavity with two chlorido ligands in apical positions forming distorted pentagonal bipyramidal coordination sphere, while in complexes **5** and **6** the ligand is extensively folded, and the metal, with coordinated one and two chlorido ligands, respectively, adopts distorted square pyramidal geometry. Along the series of the complexes (**1**−**6**), the metal−nitrogen atom distances are reduced from ∼2.2 to ∼2.0 Å, while the metal−oxygen atom distances are elongated, so that both the oxygens are semicoordinated (2.506(3) and 2.663(3) Å) in **4**. On the other hand, one oxygen is semicoordinated (2.721(2) Å), and the second one stays uncoordinated (3.816(2) Å) in **5**, whereas both oxygen atoms are considered as uncoordinated (3.113(2) and 4.030(2) Å) in **6**. Therefore the coordination number is reduced from 7 for **1**−**3** or 5 + 2 for **4** to 4 + 1 for **5** or 5 for **6**. The findings regarding the bond character were also supported by DFT calculations using the Mayer's bond order and electron localization function. The observed changes in stereochemistry may be related to a variation of the ionic radius of the changing metal ion within the series going from Mn (**1**) to Zn (**6**), because the macrocyclic cavity becomes too large for smaller metal ions, and thus, the ligand is folded with liberation/decoordination of the oxygen donor atom(s). The type of the central metal atom as well as its ionic radius also influences significantly magnetic properties of the complexes from which the parameters describing magnetic anisotropy and intermolecular magnetic exchange were extracted. Complexes **1** and **2** behave as expected for $3d^5$ spin configuration. For **3**, a large positive value of $D \approx 40$ cm^{-1} was found, also with a very small negative J-value. For **4**, the best fit of data was obtained for 1D chain model giving a relatively large negative value of D = −6.02 cm^{-1}, non-negligible value of rhombicity (E/D = 0.15), and small antiferromagnetic exchange coupling, with J = −0.48 cm^{-1}. In the case of **5**, the best fit was provided using 1D chain model, which revealed the largest antiferromagnetic exchange, with J = −2.43 cm^{-1}. According to the obtained results, the discussed complexes can be sorted by increasing antiferromagnetic exchange as follows: Co(II) < Mn(II) < Fe(III) < Ni(II) < Cu(II). The obtained ZFS parameters were correlated well with ab initio calculations (SA-CASSCF NEVPT2), and the energy difference Δ between BS and HS states as well as exchange constants J (B3LYP+ZORA/def2-TZVP(-f)) were calculated for all the possible M···M distances to reveal the magnetic interactions through noncovalent superexchange pathways. The strongest magnetic interactions were found for the shortest M···M distances where the two complex units are connected via a network of strong hydrogen bonds (complexes **1**, **2**, and **4**). On the other hand, the largest antiferromagnetic exchange in Cu(II) complex **5** was found for the almost largest Cu···Cu distance, mediated by C−H···Cl hydrogen bond. To conclude, the presented work showed that mutual cooperation between experimental techniques and theoretical methods is essential for better understanding of electronic and magnetic properties of coordination compounds based on 15-membered pyridine-based macrocycle ligand **L**.

ASSOCIATED CONTENT

Supporting Information

FTIR spectra (**1**−**6**), results of TG/DTA analysis (**1** and **3**), figures and tables referring to the X-ray analysis, magnetic data analysis, and calculated results. This material is available free of charge via the Internet at http://pubs.acs.org.

AUTHOR INFORMATION

Corresponding Author

*Fax: +420 585634954. Phone: +420 585634352. E-mail: zdenek.travnicek@upol.cz.

Notes

The authors declare no competing financial interest.

ACKNOWLEDGMENTS

Authors gratefully thank for the financial support the Czech Science Foundation (Grant No. 13-32167P) and the National Program of Sustainability (NPU LO1305) of the Ministry of Education, Youth, and Sports of the Czech Republic.

DOI: 10.1021/ic503054m
Inorg. Chem. 2015, 54, 3352−3369

REFERENCES

(1) Allen, F. H. *Acta Crystallogr.* **2002**, *B58*, 380−388.
(2) Drew, M. G. B.; bin Othman, A. H.; McFall, S. G.; Mcllroy, P. D. A.; Nelson, S. M. *J. Chem. Soc., Dalton Trans.* **1977**, *12*, 1173−1180.
(3) Cook, D. H.; Fenton, D. E.; Drew, M. G. B.; McFall, S. G.; Nelson, S. M. *J. Chem. Soc., Dalton Trans.* **1977**, *5*, 446−449.
(4) Nelson, S. M.; Mcllroy, P. D. A.; Stevenson, C. S.; Konig, E.; Ritter, G.; Waigel, J. *J. Chem. Soc., Dalton Trans.* **1986**, *5*, 991−995.
(5) König, E.; Ritter, G.; Dengler, J.; Nelson, S. M. *Inorg. Chem.* **1987**, *26*, 3582−3588.
(6) Radeckaparyzek, W.; Patroniakkrzyminiewska, V. *Polyhedron* **1995**, *14*, 2059−2062.
(7) Patroniak-Krzyminiewska, V.; Radecka-Paryzek, W. *Collect. Czech. Chem. Commun.* **1998**, *63*, 363−370.
(8) Hayami, S.; Gu, Z.; Einaga, Y.; Kobayasi, Y.; Ishikawa, Y.; Yamada, Y.; Fujishima, A.; Sato, O. *Inorg. Chem.* **2001**, *40*, 3240−3242.
(9) Bonadio, F.; Senna, M.-C.; Ensling, J.; Sieber, A.; Neels, A.; Stoeckli-Evans, H.; Decurtins, S. *Inorg. Chem.* **2005**, *44*, 969−978.
(10) Hayami, S.; Juhász, G.; Maeda, Y.; Yokoyama, T.; Sato, O. *Inorg. Chem.* **2005**, *44*, 7289−91.
(11) Bonhommeau, S.; Guillon, T.; Lawson Daku, L. M.; Demont, P.; Sanchez Costa, J.; Létard, J. F.; Molnár, G.; Bousseksou, A. *Angew. Chem., Int. Ed. Engl.* **2006**, *45*, 1625−1629.
(12) Paraschiv, C.; Andruh, M.; Journaux, Y.; Žak, Z.; Kyritsakas, N.; Ricard, L. *J. Mater. Chem.* **2006**, *16*, 2660−2668.
(13) Guionneau, P.; Le Gac, F.; Kaiba, A.; Costa, J. S.; Chasseau, D.; Létard, J. F. *Chem. Commun.* **2007**, *36*, 3723−3725.
(14) Zhang, D.; Wang, H.; Chen, Y.; Ni, Z. H.; Tian, L.; Jiang, J. *Inorg. Chem.* **2009**, *48*, 5488−5496.
(15) Zhang, D.; Wang, H.; Chen, Y.; Zhang, L.; Tian, L.; Ni, Z. H.; Jiang, J. *Dalton Trans.* **2009**, *43*, 9418−9425.
(16) Zhang, D.; Wang, H.; Tian, L.; Jiang, J.; Ni, Z.-H. *Cryst. Eng. Comm.* **2009**, *11*, 2447−2451.
(17) Zhang, Y. Z.; Sato, O. *Inorg. Chem.* **2010**, *49* (4), 1271−1273.
(18) Zhang, Y. Z.; Wang, B. W.; Sato, O.; Gao, S. *Chem. Commun.* **2010**, *46*, 6959−6961.
(19) Lüning, U.; Petersen, S.; Schyja, W.; Hacker, W.; Marquardt, T.; Wagner, K.; Bolte, M. *Eur. J. Org. Chem.* **1998**, 1077−1084.
(20) Storm, O.; Lüning, U. *Chem.—Eur. J.* **2002**, *8*, 793−798.
(21) Wessjohann, L. A.; Rivera, D. G.; León, F. *Org. Lett.* **2007**, *9*, 4733−4736.
(22) Drahoš, B.; Kotek, J.; Hermann, P.; Lukeš, I.; Tóth, E. *Inorg. Chem.* **2010**, *49*, 3224−3238.
(23) Gryko, D. T.; Piatek, P.; Pecak, A.; Palys, M.; Jurczak, J. *Tetrahedron* **1998**, *54*, 7505−7516.
(24) Szumna, A.; Gryko, D. T.; Jurczak, J. *J. Chem. Soc., Perkin Trans. 2* **2000**, 1553−1558.
(25) Gryko, D.; Gryko, D. T.; Sierzputowska-Gracz, H.; Piatek, P.; Jurczak, J. *Helv. Chim. Acta* **2004**, *87*, 156−166.
(26) Latouche, C.; Lanoë, P.-H.; Williams, J. A. G.; Guerchais, V.; Boucekkine, A.; Fillaut, J.-L. *New J. Chem.* **2011**, *35*, 2196−2202.
(27) Oshchepkov, M. S.; Perevalov, V. P.; Kuzmina, L. G.; Anisimov, A. V.; Fedorova, O. A. *Russ. Chem. Bull.* **2011**, *60*, 478−485.
(28) Fedorova, O.; Fedorov, Y.; Oshchepkov, M. *Electroanalysis* **2012**, *24*, 1739−1744.
(29) Wang, J.; Slater, B.; Alberola, A.; Stoeckli-Evans, H.; Razavi, F. S.; Pilkington, M. *Inorg. Chem.* **2007**, *46*, 4763−4765.
(30) Fenton, D. E.; Murphy, B. P.; Leong, A. J.; Lindoy, L. F.; Bashall, A.; Mcpartlin, M. *J. Chem. Soc., Dalton Trans.* **1987**, 2543−2553.
(31) Korendovych, I. V.; Staples, R. J.; Reiff, W. M.; Rybak-Akimova, E. V. *Inorg. Chem.* **2004**, *43*, 3930−3941.
(32) Korendovych, I. V.; Kryatova, O. P.; Reiff, W. M.; Rybak-Akimova, E. V. *Inorg. Chem.* **2007**, *46*, 4197−4211.
(33) Platas-Iglesias, C.; Vaiana, L.; Esteban-Gómez, D.; Avecilla, F.; Real, J. A.; de Blas, A.; Rodríguez-Blas, T. *Inorg. Chem.* **2005**, *44*, 9704−9713.
(34) Vaiana, L.; Regueiro-Figueroa, M.; Mato-Iglesias, M.; Platas-Iglesias, C.; Esteban-Gómez, D.; de Blas, A.; Rodríguez-Blas, T. *Inorg. Chem.* **2007**, *46*, 8271−8282.
(35) Ruamps, R.; Batchelor, L. J.; Maurice, R.; Gogoi, N.; Jiménez-Lozano, P.; Guihéry, N.; de Graaf, C.; Barra, A.-L.; Sutter, J.-P.; Mallah, T. *Chem. Eur. J.* **2013**, *19*, 950−956.
(36) Gogoi, N.; Thlijeni, M.; Duhayon, C.; Sutter, J.-P. *Inorg. Chem.* **2013**, *52*, 2283−2285.
(37) Boča, R. *Theoretical Foundations of Molecular Magnetism;* Elsevier: Amsterdam, 1999.
(38) *CrysAlis CCD and CrysAlis RED,* Version 1.171.33.52; Oxford Diffraction Ltd.: England, 2009.
(39) Sheldrick, G. M. *Acta Crystallogr., Sect. A: Found. Crystallogr.* **2008**, *64*, 112−122.
(40) (a) Macrae, C. F.; Bruno, I. J.; Chisholm, J. A.; Edgington, P. R.; McCabe, P.; Pidcock, E.; Rodriguez-Monge, L.; Taylor, R.; van de Streek, J.; Wood, P. A. *J. Appl. Crystallogr.* **2008**, *41* (2), 466−470. (b) Brandenburg, K. *DIAMOND,* Release 3.2k; Crystal Impact GbR: Bonn, Germany, 2014.
(41) Neese, F. *WIREs Comput. Mol. Sci.* **2012**, *2*, 73−78.
(42) Pantazis, D. A.; Chen, X. Y.; Landis, C. R.; Neese, F. *J. Chem. Theory Comput.* **2008**, *4*, 908−919.
(43) (a) van Lenthe, E.; Baerends, E. J.; Snijders, J. G. *J. Chem. Phys.* **1993**, *99*, 4597−4610. (b) van Wullen, C. *J. Chem. Phys.* **1998**, *109*, 392−399.
(44) (a) Lee, C.; Yang, W.; Parr, R. G. *Phys. Rev. B* **1988**, *37*, 785−789. (b) Becke, A. D. *J. Chem. Phys.* **1993**, *98*, 1372−1377. (c) Becke, A. D. *J. Chem. Phys.* **1993**, *98*, 5648−5652. (d) Stephens, P. J.; Devlin, F. J.; Chabalowski, C. F.; Frisch, M. J. *J. Phys. Chem.* **1994**, *98*, 11623−11627.
(45) (a) Ruiz, E.; Cano, J.; Alvarez, S.; Alemany, P. *J. Comput. Chem.* **1999**, *20*, 1391−1400. (b) Ruiz, E.; Rodríguez-Fortea, A.; Cano, J.; Alvarez, S.; Alemany, P. *J. Comput. Chem.* **2003**, *24*, 982−989.
(46) (a) Yamaguchi, K.; Takahara, Y.; Fueno, T. Ab Initio Molecular Orbital Studies of Structure and Reactivity of Transition Metal-OXO Compounds. In *Applied Quantum Chemistry;* Smith, V. H., Schaefer, H. F., Morokuma, F., Eds.; Reidel: Dordrecht, The Netherlands, 1986; pp 155−184. (b) Soda, T.; Kitagawa, Y.; Onishi, T.; Takano, Y.; Shigeta, Y.; Nagao, H.; Yoshioka, Y.; Yamaguchi, K. *Chem. Phys. Lett.* **2000**, *319*, 223−230.
(47) (a) Grimme, S.; Antony, J.; Ehrlich, S.; Krieg, H. *J. Chem. Phys.* **2010**, *132*, 154104. (b) Grimme, S.; Ehrlich, S.; Goerigk, L. *J. Comput. Chem.* **2011**, *32*, 1456−1465.
(48) Malmqvist, P. A.; Roos, B. O. *Chem. Phys. Lett.* **1989**, *155*, 189−194.
(49) (a) Angeli, C.; Cimiraglia, R.; Evangelisti, S.; Leininger, T.; Malrieu, J. P. *J. Chem. Phys.* **2001**, *114*, 10252−10264. (b) Angeli, C.; Cimiraglia, R.; Malrieu, J. P. *Chem. Phys. Lett.* **2001**, *350*, 297−305. (c) Angeli, C.; Cimiraglia, R.; Malrieu, J. P. *J. Chem. Phys.* **2002**, *117*, 9138−9153. (d) Angeli, C.; Borini, S.; Cestari, M.; Cimiraglia, R. *J. Chem. Phys.* **2004**, *121*, 4043−4049. (e) Angeli, C.; Bories, B.; Cavallini, A.; Cimiraglia, R. *J. Chem. Phys.* **2006**, *124*, 054108.
(50) Ganyushin, D.; Neese, F. *J. Chem. Phys.* **2006**, *125*, 024103.
(51) Neese, F. *J. Chem. Phys.* **2005**, *122*, 034107.
(52) Maurice, R.; Bastardis, R.; Graaf, C.; Suaud, N.; Mallah, T.; Guihéry, N. *J. Chem. Theory Comput.* **2009**, *5*, 2977−2984.
(53) (a) Neese, F.; Wennmohs, F.; Hansen, A.; Becker, U. *Chem. Phys.* **2009**, *356*, 98−109. (b) Izsak, R.; Neese, F. *J. Chem. Phys.* **2011**, *135*, 144105.
(54) Lu, T.; Chen, F. *J. Comput. Chem.* **2012**, *33*, 580−592.
(55) Mayer, I. *Chem. Phys. Lett.* **1983**, *97*, 270−274.
(56) (a) Becke, A. D.; Edgecombe, K. E. *J. Chem. Phys.* **1990**, *92*, 5397. (b) Lu, T.; Chen, F.-W. *Acta Phys.-Chim. Sin.* **2011**, *27*, 2786−2792.
(57) *The Quantum Theory of Atoms in Molecules: From Solid State to DNA and Drug Design;* Matta, C. F., Boyd, R. J., Eds; Wiley-VCH: Weinheim, Germany, 2007.
(58) Allouche, A. R. *J. Comput. Chem.* **2011**, *32*, 174−182.

DOI: 10.1021/ic503054m
Inorg. Chem. 2015, 54, 3352−3369

(59) *POV-Ray 3.6;* Persistence of Vision Raytracer Pty. Ltd.: Williamstown, Victoria, Australia, 2004.
(60) Jimenez-Sandoval, O.; Ramirez-Rosales, D.; Rosales-Hoz, M. D.; Sosa-Torres, M. E.; Zamorano-Ulloa, R. *J. Chem. Soc., Dalton Trans.* **1998**, 1551−1556.
(61) Keypour, H.; Khanmohammadi, H.; wainwright, K. P. *Inorg. Chim. Acta* **2003**, *355*, 286−291.
(62) Fleischer, E.; Hawkinson, S. *Inorg. Chem.* **1967**, *89*, 720−721.
(63) Drew, M. G. B.; Hamid bin Othman, A.; Martin Nelson, S. *J. Chem. Soc., Dalton Trans.* **1976**, 1394−1399.
(64) Venkatakrishnan, T. S.; Sahoo, S.; Brefuel, N.; Duhayon, C.; Paulsen, C.; Barra, A. L.; Ramasesha, S.; Sutter, J. P. *J. Am. Chem. Soc.* **2010**, *132*, 6047−6056.
(65) Drew, M. G. B.; Hollis, S.; Yates, P. C. *J. Chem. Soc., Dalton. Trans.* **1985**, 1829−1834.
(66) Rakowski, M. C.; Rycheck, M.; Busch, D. H. *Inorg. Chem.* **1975**, *14*, 1194−1200.
(67) Alcock, N. W.; Moore, P.; Omar, H. A. A.; Reader, C. J. *J. Chem. Soc., Dalton Trans.* **1987**, 2643−2648.
(68) Addison, A. W.; Rao, T. N.; Reedjik, J.; van Rijn, J.; Verschoor, G. C. *J. Chem. Soc., Dalton Trans.* **1984**, 1349−1356.
(69) Fernandes, A. S.; Cabral, M. F.; Costa, J.; Castro, M.; Delgado, R.; Drew, M. G.; Felix, V. *J. Inorg. Biochem.* **2011**, *105*, 410−419.
(70) XDrew, M. G. B.; Neison, S. H. *Acta Crystallogr., Sect. A: Cryst. Phys., Diffr., Theor. Gen. Crystallogr.* **1975**, *31*, S140−S140.
(71) Shannon, R. D. *Acta Crystallogr.* **1976**, *A32*, 751−767.
(72) Regueiro-Figueroa, M.; Lima, L. M. P.; Blanco, V.; Esteban-Gómez, D.; de Blas, A.; Rodríguez-Blas, T.; Delgado, R.; Platas-Iglesias, C. *Inorg. Chem.* **2014**, *53*, 12859−12869.
(73) (a) Alvarez, S. *Dalton Trans.* **2005**, 2209−2233. (b) Casanova, D.; Alemany, P.; Bofill, J. M.; Alvarez, S. *Chem.—Eur. J.* **2003**, *9*, 1281−1295.
(74) Herchel, R.; Šindelář, Z.; Trávníček, Z.; Zbořil, R.; Vančo, J. *Dalton Trans.* **2009**, 9870−9880.
(75) (a) Herchel, R.; Pavelek, L.; Trávníček, Z. *Dalton Trans.* **2011**, *40*, 11896−11903. (b) Šalitroš, I.; Boča, R.; Herchel, R.; Moncol, J.; Nemec, I.; Ruben, M.; Renz, F. *Inorg. Chem.* **2012**, *51*, 12755−12767.
(76) Waldmann, O. *Phys. Rev. B: Condens. Matter Mater. Phys.* **2000**, *61*, 6138−6144.
(77) Bradley, C. J.; Cracknell, A. P. *The Mathematical Theory of Symmetry in Solids;* Clarendon Press: Oxford, U.K., 1972.
(78) Nemec, I.; Herchel, R.; Šalitroš, I.; Trávníček, Z.; Moncol, J.; Fuess, H.; Ruben, M.; Linert, W. *CrystEngComm* **2012**, *14*, 7015−7024.
(79) (a) Evans, J. F. D. *J. Chem. Soc.* **1959**, 2003. (b) Olatunde, A. O.; Cox, J. M.; Daddario, M. D.; Spernyak, J. A.; Benedict, J. B.; Morrow, J. R. *Inorg. Chem.* **2014**, *53*, 8311−8321.

DOI: 10.1021/ic503054m
Inorg. Chem. 2015, 54, 3352−3369